Electronic Supplementary Material (ESI) for Nanoscale.

Supporting Information

On the of optical anisotropy in 2D metal-halide perovskites

Mark Steger,[1#] Svenja M. Janke,[2,3,4,#] Peter C. Sercel,[5,#] Bryon W. Larson,[1] Haipeng Lu,[1,6] Xixi Qin,[2] Victor Wen-zhe Yu,[2] Volker Blum,[2,7] Jeffrey L. Blackburn[1*]*

1. National Renewable Energy Laboratory, Golden, CO 80401
2. Thomas Lord Department of Mechanical Engineering and Materials Science, Duke University, Durham, NC 27708
3. The Institute for Advanced Study, University of Warwick, CV4 7AL Coventry, United Kingdom
4. Department of Chemistry, University of Warwick, Coventry, CV4 7AL, United Kingdom
5. Center for Hybrid Organic Inorganic Semiconductors for Energy, Golden, CO, 80401 USA
6. Department of Chemistry, The Hong Kong University of Science and Technology, Clear Water Bay, Hong Kong
7. Chemistry Department, Duke University, Durham, NC 27708

\# Equal Contributions

* Corresponding Author E-mails: mark.steger@nrel.gov ; Jeffrey.blackburn@nrel.gov

Contents

List of Figures

List of Tables

Section S1. Details of Ellipsometry Modeling

Section S1.1 Note on Simultaneous Fitting of Multimode Ellipsometry

The three datasets (transmittance (T), reflection ellipsometry (rSE) and transmission ellipsometry (tSE)) are fit simultaneously and self-consistently to maximize sensitivity to the in-plane and out-of-plane optical constants for the film. Specifically, we are fitting datasets that obey different functional relationships on the same set of parameters. i.e.

$$rSE = f(\boldsymbol{h\nu}, \boldsymbol{\theta}, \boldsymbol{p_1}, \boldsymbol{p_2}, \boldsymbol{p_3}, \dots) \tag{S1}$$

$$tSE = g(\boldsymbol{h\nu}, \boldsymbol{\theta}, \boldsymbol{p_1}, \boldsymbol{p_2}, \boldsymbol{p_3}, \dots) \tag{S2}$$

$$T = h(\boldsymbol{h\nu}, \boldsymbol{\theta}, \boldsymbol{p_1}, \boldsymbol{p_2}, \boldsymbol{p_3}, \dots) \tag{S3}$$

Using CompleteEASE, we sum the residuals of all three data sets to minimize the errors across all data sets simultaneously for a single set of $\{\boldsymbol{p_i}\}$**.** In practice, rSE is very sensitive to thickness and surface quality, and T is helpful in reducing correlations between thickness and k of the ordinary axis (but taken at $\boldsymbol{\theta = 0}$**,** is insensitive to the extraordinary absorption). By adding tSE, we see a further reduction in correlations between ordinary and extraordinary absorptions [1]. Further, we analyze multiple samples of both thin film and cleaved crystals. Again, we use self-consistency between multiple samples of different thickness to ensure representative results and reduce potential correlations between thickness and optical constants.

Section S1.2 General Oscillator Model

The full oscillator model used for the thin film are presented in Figure S1. Here, we note that all oscillators are modeled as Gaussians, except for a broad peak just above the excitons that we fit with a PSemiM0. We include a calculation of ε_1 with the excitonic contribution to ε_2 removed to highlight the importance of the exciton to the background index in the transparent region.

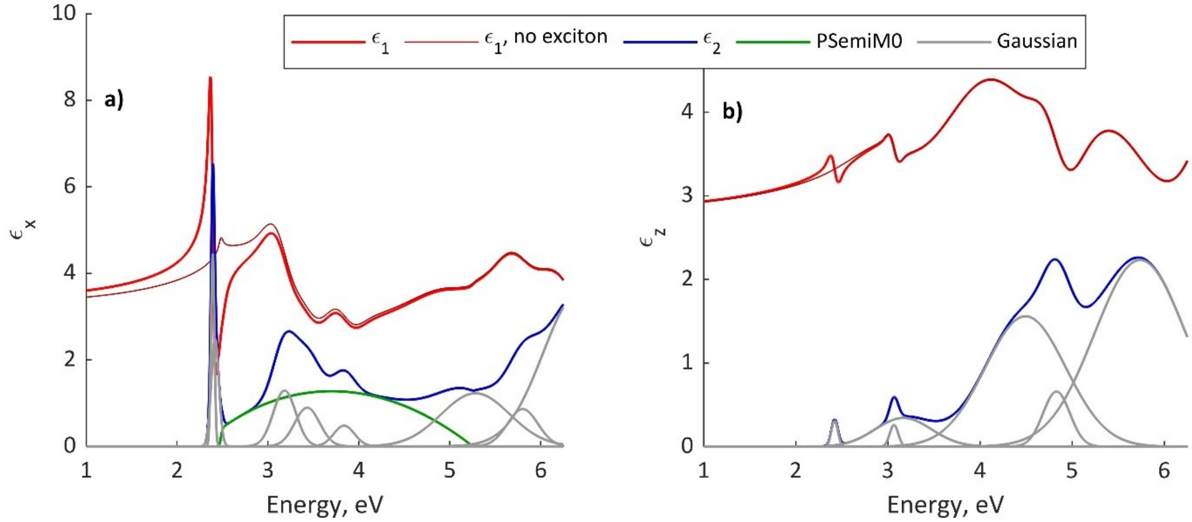

Figure S1 General oscillator uniaxial model. (a) ordinary axis. (b) extraordinary axis.

Section S1.3 Note on Excitonic model

The exciton was modeled with Gaussian oscillators in the range of 2.38-2.5eV below a PSemiM0 direct band gap model with turn on around 2.48-2.6 eV. The ordinary axis of the thin film is modeled with 2 Gaussians. The cleaved crystal exciton appears sharper and is modeled with 3 Gaussians. When modeled as anisotropic, only one Gaussian is ever used for the out of plane component.

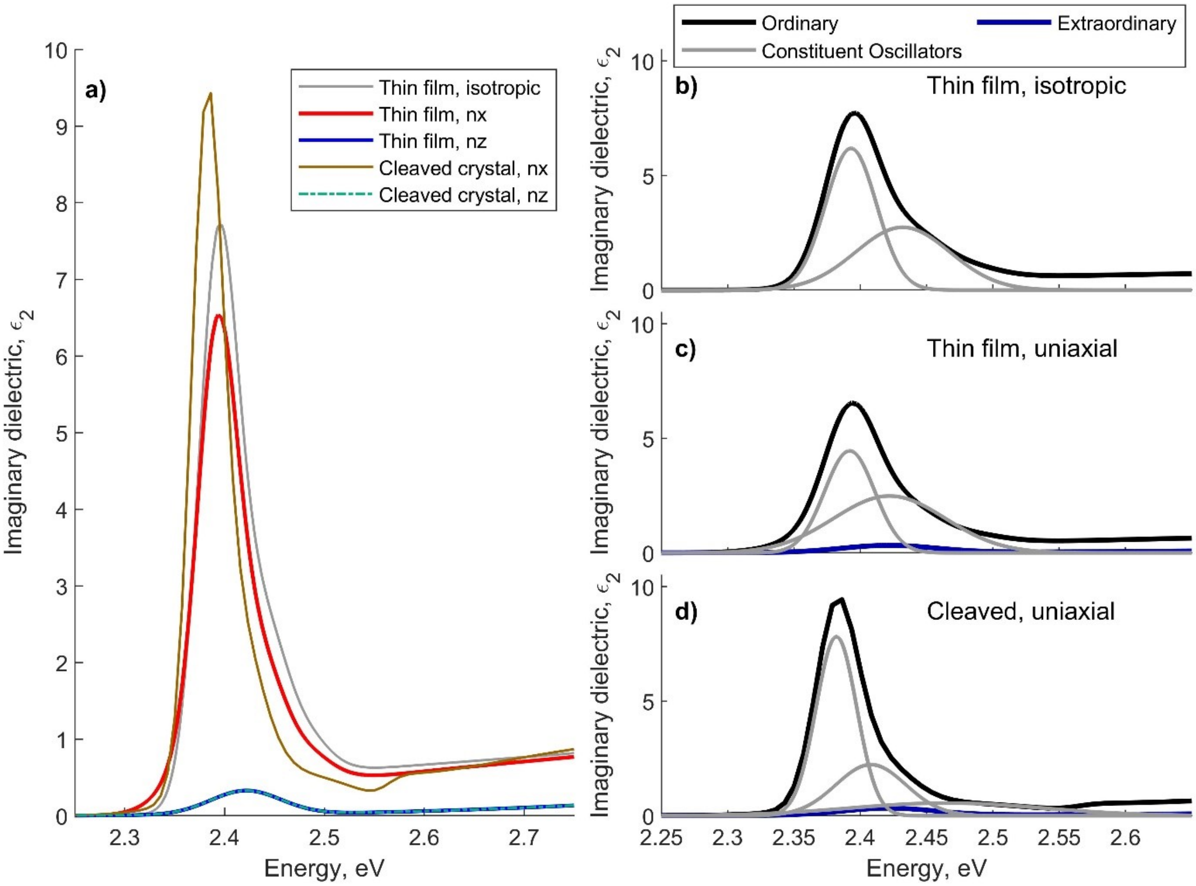

Figure S2. Modeled excitonic absorption, ϵ_2. **a**: a direct comparison of the total absorption around the band gap. The strong anisotropy between IP and OP is manifest. Also, we see a sharper exciton from the cleaved crystal, as well as a sharper absorption turn-on close to 2.6 eV. While this shape is anthropogenic—enforced by the choice of oscillator functions—we do resolve a clear change in the shape of the absorption relative to the thin film. **b-c**: the model is expressed in terms of the constituent Gaussian oscillators for the three models.

Section S1.4 Confidence intervals on modeled optical constants

We estimate the uncertainty on the model by accounting for systematic errors. This is done in CompleteEASE using the Fit Error Magnitude function, and this is distinct from the much smaller 90% confidence intervals derived for random errors. The systematic error is used to calculate a confidence range on the model, i.e. a range of acceptable models that fit the data. These confidence ranges are plotted in Fig. S3. It is immediately obvious that confidence on ordinary axis ε is generally much better than that on the extraordinary axis. Also, we see that the absolute confidence in the isotropic model is worse than the corresponding uniaxial model, a natural consequence of the relative goodness of the fit. Lastly, we note that the crystal model (frames c and f) underestimates the confidence interval on the extraordinary axis because we fit the critical point parameters in that analysis to those derived for the thin film.

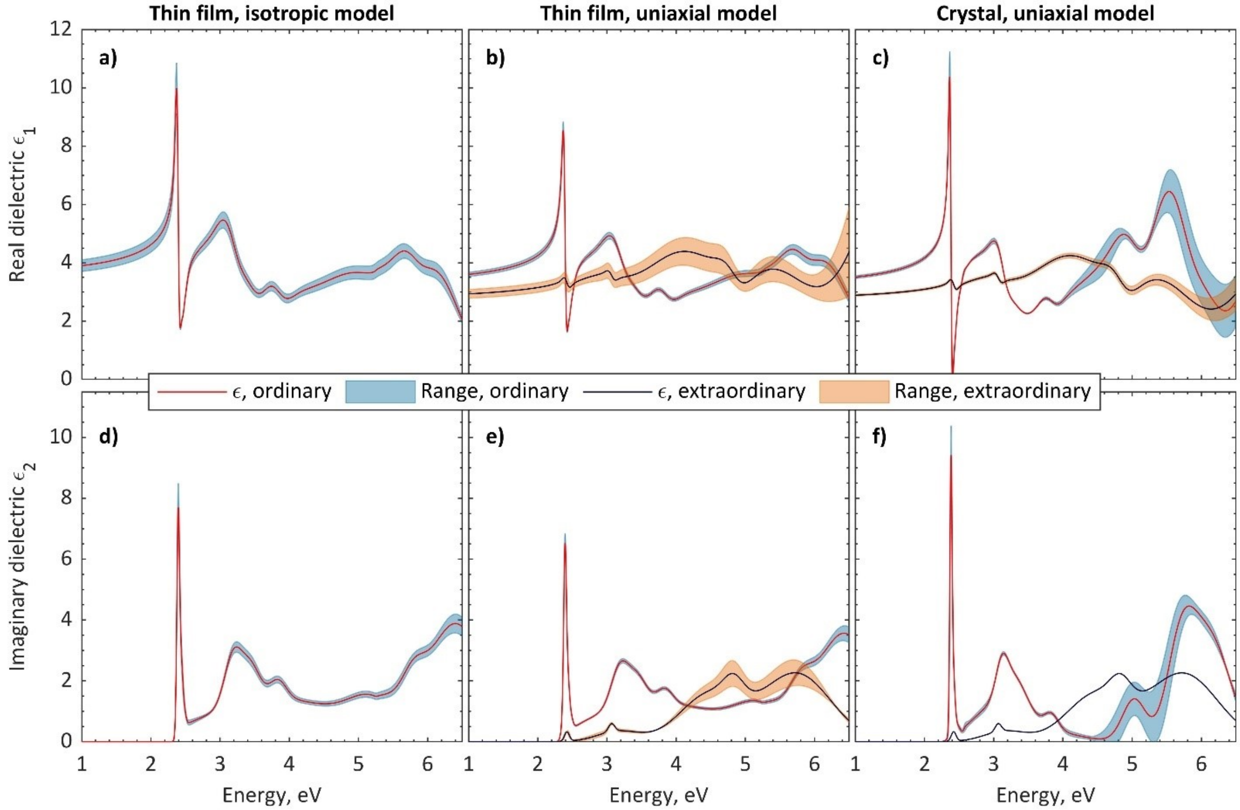
Thin film, isotropic model
Thin film, uniaxial model
Crystal, uniaxial model

Figure S3. Modeled dielectric functions, with fit parameter uncertainties propagated to dielectric models. (a) and (d) the inaccurate isotropic model shows a large uncertainty in the extracted dielectric function due to the inadequacy of the model. (b) and (e) the uniaxial model greatly improves precision in the ordinary axis, but we see the extraordinary component is less certain. For the cleaved crystal, (c) and (f), we fix the critical points of the extraordinary, so no confidence is computed for that parameter. The very large uncertainty in the UV can be attributed to the high roughness of the sample. On the other hand, the birefringence is more precisely determined due back reflections in the thick, high-quality crystal.

Section S2. Details of DFT Calculations

Table S1. Comparison of the DFT-PBE [2] plus Tkatchenko-Scheffler (TS) van-der-Waals correction [3] lattice parameters of PEPI to experimentally measured values. In the computations, the crystallographic ***a*** axis corresponds to the long axis perpendicular to the inorganic layer. In the second row of the table, the axes labels are swapped to match the convention used for the experimental values. The ***c***-lattice vector is either given for unit cells with two or one inorganic layer. In the comparison to the unit cells containing only one inorganic layer, we double the unit cell parameter ***c***, because the unit cell used in the present computations contains two inorganic layers. The computed lattice parameters deviate from the low-temperature measurements by less than 1%. Deviation from higher temperature measurements is larger (up to 3 %) and is expected, since DFT-PBE+TS does not include temperature effects; we also note that there is some discrepancy between different experiments. Likewise, there appears to be some discrepancy regarding unit cell angles between different reports. While the same angle can be reported as either >90° or <90° (e.g., in different reports of the α angle), some larger deviations appear between different reported experimental values of the β angle. Our computational results match the experimentally reported results in Refs. [4,5].

Ref.	***a***	***b***	***c***	α	β	γ
DFT-PBE+TS (choice of axis labels in computation)	32.36 Å	8.66 Å	8.70 Å	89°	86°	85°
DFT-PBE+TS (axes swapped to allow comparison to literature)	8.70 Å	8.66 Å	32.36 Å	85°	86°	89°
Ref. [6] 100K	8.679(2) Å	8.684(2) Å	16.410(4) Å	94.453(14)°	100.588(13)°	90.573(11)°
Dev. (%)	0.24	0.28	1.42	0.64	7.66	1.77
Ref. [4] 100 K	8.6863(2) Å	8.6856(2) Å	32.3872(8) Å	85.2360(10)°	85.2760(10)°	89.4460(2)°
Dev. (%)	0.16	0.30	0.08	0.28	0.85	0.50
Ref. [4] 300 K	8.7437(2) Å	8.7437(2) Å	33.0253(6) Å	84.6160(9)°	84.6307(9)°	89.6320(9)°
Dev. (%)	0.50	0.97	2.06	0.45	1.59	0.71
Ref. [5] 296 K	8.7389(2) Å	8.7403(2) Å	32.9952(6) Å	84.646(1)°	85.657(1)°	89.643(1)°
Dev. (%)	0.45	0.93	1.96	0.42	0.40	0.72
Ref. [7]	8.734 Å	8.747 Å	16.682 Å	95.19°	99.79°	90.34°
Dev. (%)	0.39	1.00	3.10	0.22	6.73	1.51

Section S2.1 Note on Underestimation of the computed band gap by HSE06 + SOC

The underestimation of the computed band gap (2.01 eV), relative to the range of experimental estimates of the fundamental gap (~2.5-2.8 eV [8–14]), is an expected systematic error of the HSE06+SOC method. It combines (i) an underestimation of SOC by the second-variational approach, which we have quantified previously [15,16], and (ii) the known uncertainty of hybrid density functionals when used to estimate the fundamental gaps of semiconductors. One approach that is sometimes applied for homogeneous (i.e., non-hybrid) materials is to optimize the exchange mixing parameter in the hybrid functional to simply match the experimentally observed fundamental gap. In the present case, this strategy is not directly applicable since the exact fundamental gap of PEPI is not known (the position of the exciton is well established, but different estimates exist for the exciton binding energy and fundamental gap, which are harder to measure). More importantly, adjusting the hybrid functional by a single, spatially homogeneous parametrization cannot account for the presence of separate organic and inorganic components, which would necessitate the use of different mixing parameters to match their respective fundamental gaps. As we have done successfully in past work, we instead avoid any material-specific parameterization of the exchange mixing parameter, accepting the unavoidable systematic error of a hybrid functional while retaining relative comparability of our results to those obtained for other hybrid materials when treated with the same approach. In past work, have found that the HSE06 mixing parameter $\alpha = 0.25$ can reproduce experimentally observed level alignments near the band edges satisfactorily for layered organic-inorganic perovskites (see e.g. Ref [17]).

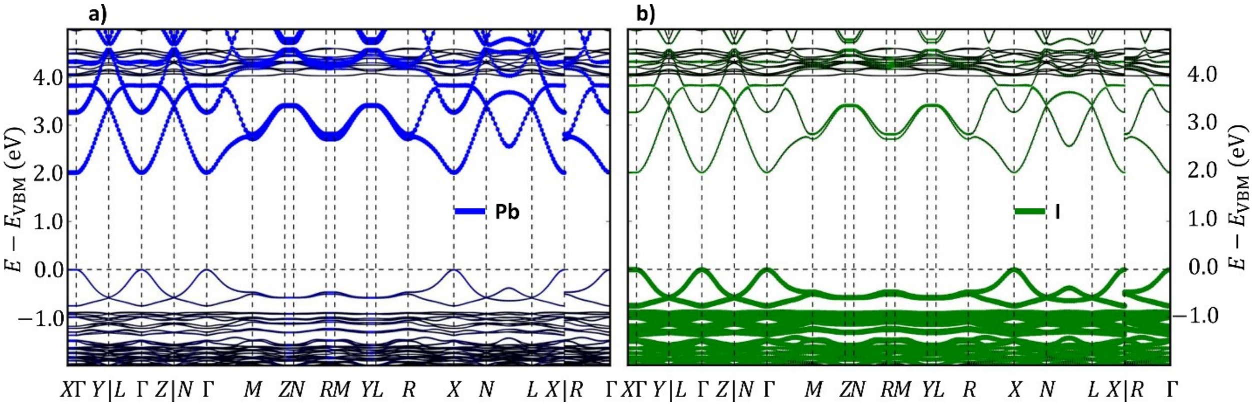

Figure S4. DFT-HSE06+SOC band structure for $(\mathrm{PEA})_2\mathrm{PbI}_4$. The contribution of a) Pb (blue) and b) of I (green) to the frontier orbitals is indicated. The band gap is direct at Γ and amounts to 2.01 eV.

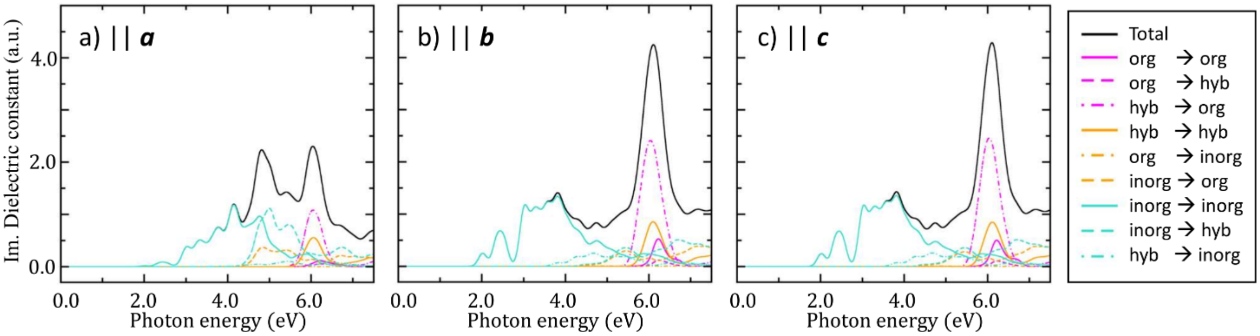

Figure S5. Decomposition of the DFT-HSE06 [18] plus SOC [15] total dielectric constant (dashed black) for the different crystallographic directions as a function of the photon energy into transitions starting and ending in orbitals of the following characters: organic-organic (magenta solid), organic-hybrid (magenta dashed), hybrid-organic (magenta dash-dotted); inorganic-inorganic (cyan solid), inorganic-hybrid (cyan dashed), hybrid-inorganic (cyan dash-dotted); hybrid-hybrid (orange solid), organic-inorganic (orange dashed), inorganic-organic (orange dash-dotted). The character of the DFT orbitals is determined by a Mulliken decomposition of each orbital into contributions from the organic and inorganic framework, respectively. Orbitals that are more than 80% localized on a single component are denoted as organic or inorganic, respectively, whereas orbitals that are significantly extended across both components are denoted as "hybrid" (hyb) (see Fig. S6 for an example). The dipole operator is local, so any transitions between orbitals that are predominantly assigned to different spatial regions must happen in regions in which those orbitals overlap.

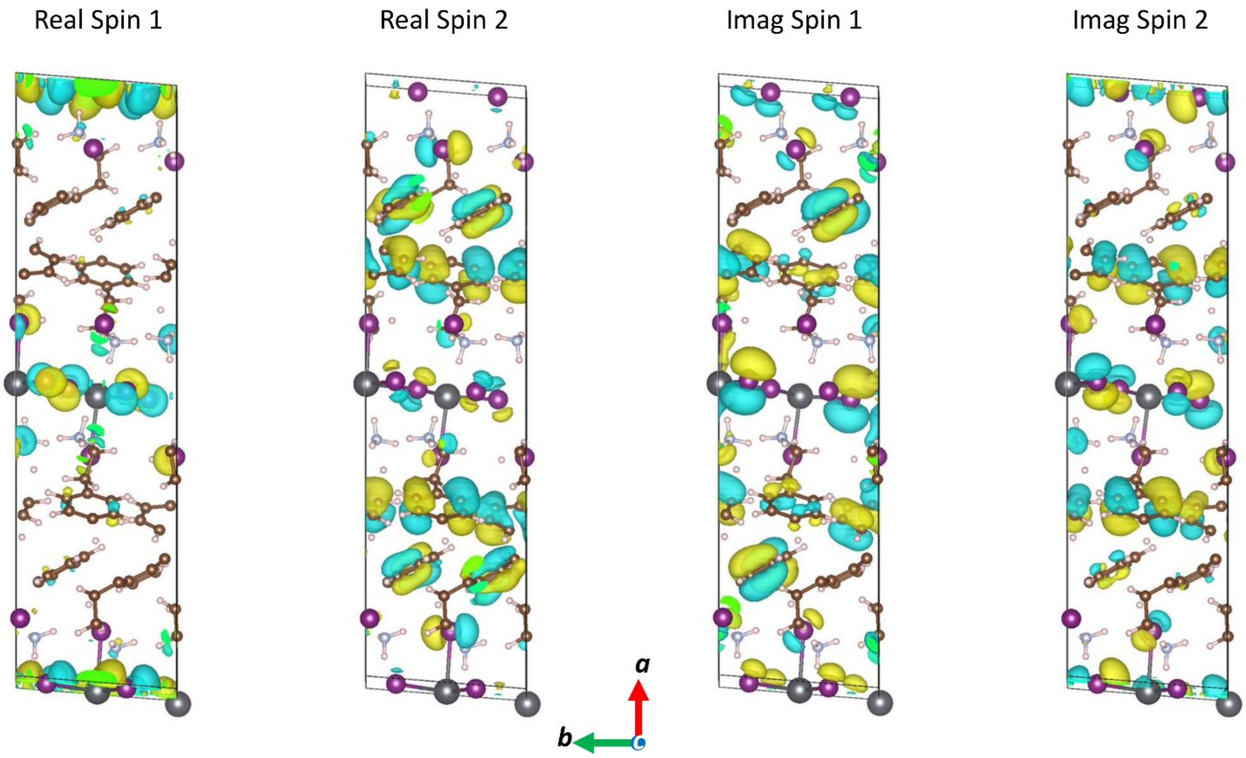

Figure S6. Example of a "hybrid" DFT orbital that is extended across both the organic and the inorganic component, rather than being localized on just one of the components. Orbital (eigenstate 1635 at -1.664 eV below the VBM) at Γ point calculated with DFT-HSE06+SOC. The real and imaginary part of the first and second spinor wave function are shown.

Section S2.2 Note on computed band edge effective masses by HSE06 + SOC and PBE+SOC

From the energy band structures computed for $(PEA)_2PbI_4$ using DFT-HSE06+SOC, shown in Fig S4, we computed the Γ point effective masses for in-plane dispersion along the ΓY, ΓZ, and ΓM paths in k-space. The effective masses were determined by fitting the calculated band structure to a parabolic dispersion curve over each path, 10% of the way to the Brillouin zone boundary. The unit cell used in the DFT-PBE+TS structure relaxation contains two inorganic layers, A and B, resulting from a lack of registry between adjacent inorganic layers in the X-ray-structure of Du et al. Ref [5] (see Ref. [19] for an in depth discussion of the stacking disorder in a 2D perovskite). Due to small differences in atomic positions between the two inorganic layers, the valence and conduction band are split by a small, meV-scale value for each k point. To identify which bands belong to which layer, we performed a Mulliken analysis [20]. **Table S2** shows the resulting effective masses and energy gaps computed for each band associated with the two distinct layers, as well as the computed average in-plane effective masses and the reduced effective mass for each band/layer. The computed average in-plane reduced effective mass, $\mu = 1/(1/m_e^* + 1/m_h^*)$, relevant to the discussion of excitonic effects in Section S4, is 0.110 averaged over the two layers. This value compares favorably to the experimentally measured reduced effective mass reported recently by Dyksik et al., Ref. [21].

In Section S3 we analyze the near-band edge dielectric anisotropy calculated using DFT-PBE+SOC with a (3x15x15) k-grid, denser than the grid used in the DFT-HSE06+SOC calculation, and apply the results to determine the anisotropic optical response of the exciton in Section S4. Consequently, it is important to confirm the consistency of the effective masses between the DFT-PBE+SOC and DFT-HSE06+SOC band structures. In **Table S3** we show the Γ point effective masses computed as above for in-plane dispersion along the ΓY, ΓZ and ΓM paths in k-space based on the DFT-PBE+SOC band structure. The computed average in-plane reduced effective mass, $\mu = 1/(1/m_e^* + 1/m_h^*)$, relevant to the discussion of excitonic effects in Section S4, is $\mu = 0.116\ m_0$ (where m_0 is the free electron mass) averaged over the two layers. This value is within 5% of the value determined from the DFT-HSE+SOC band structure.

Table S2. DFT-HSE06+SOC based effective masses in-plane. Effective masses m* in the table are given in units of the free electron mass and are computed near the Γ point for in-plane dispersion along the ΓY, ΓZ, and ΓM paths. They are obtained by parabolic fitting of the DFT-HSE06+SOC band structures shown in Fig. S4, 10% of the way to the respective Brillouin zone boundary, based on calculations with a (3x7x7) k-grid. The energy of each band at the Γ point with reference to the energy of the VBM is given for identification, as is an arbitrary label (A or B) denoting the distinct layer to which the corresponding band states are localized. The effective masses are nearly isotropic (with 4%) and are equal between layers (to within 1%).

	E(Γ)-E_{VBM} (eV)	m*(ΓY)	m*(ΓZ)	m*(ΓM)	Average m*	Reduced mass μ^*	
CB Layer A	2.019	0.193	0.194	0.192	0.193	Layer A	0.110
CB Layer B	2.011	0.196	0.194	0.195	0.195	Layer B	0.111
VB Layer A	0.000	0.248	0.249	0.259	0.254		
VB Layer B	-0.014	0.250	0.253	0.263	0.257	Average	0.110

Table S3. DFT-PBE+SOC based effective masses in-plane. Effective masses m* in the table are given in units of the free electron mass and are computed near the Γ point for in-plane dispersion along the ΓY, ΓZ, and ΓM paths. They are obtained by parabolic fitting of DFT-PBE+SOC band structures 10% of the way to the respective Brillouin zone boundary, based on calculations with a (3x15x15) k-grid. The energy of each band at the Γ point with reference to the energy of the VBM is given for identification, as is an arbitrary label (A or B) denoting the distinct layer to which the corresponding band states are localized. The effective masses are nearly isotropic (with 5%) and are equal between layers (to within 1%).

	E(Γ)-E_{VBM} (eV)	m*(ΓY)	m*(ΓZ)	m*(ΓM)	Average m*	Reduced mass μ^*	
CB Layer A	1.468	0.195	0.196	0.196	0.196	Layer A	0.115
CB Layer B	1.459	0.199	0.196	0.199	0.198	Layer B	0.117
VB Layer A	0.000	0.273	0.274	0.286	0.280		
VB Layer B	-0.015	0.277	0.277	0.291	0.284	Ave	0.116

Section S3. Details of K.P model for free carriers in 2D perovskites

In K.P theory, the energy band structure near the band edge at Γ is found by writing the Hamiltonian in a basis of the band edge periodic Bloch functions and then diagonalizing the Hamiltonian at non-zero wave vector $\boldsymbol{k}$. Then at any value of $\boldsymbol{k}$ the conduction and valence band states may be written approximately in the form

$$\psi_{n,\boldsymbol{k}}(\boldsymbol{r}) = u_{n,\boldsymbol{k}=0}(\boldsymbol{r})\,\frac{1}{\sqrt{V}}e^{i\,\boldsymbol{k}\cdot\boldsymbol{r}}, \tag{S4}$$

where n is a band index, $\boldsymbol{r}$ is the electron coordinate, and V is the crystal volume. In order to describe optical properties such as the transition dipole matrix element, we need expressions for the band edge Bloch functions $u_{n,\boldsymbol{k}=0}$ at $\boldsymbol{k} = 0$ for the conduction and valence bands.

For the metal halide perovskites, the valence band functions can be written as the 2-fold degenerate $J = 1/2$, $J_z = \pm 1/2$ states with S orbital symmetry: [22,23]

$$u^{v}_{\frac{1}{2},\frac{1}{2}} = S\uparrow, \qquad u^{v}_{\frac{1}{2},-\frac{1}{2}} = S\downarrow. \tag{S5}$$

Here, the symbol S denotes an orbital function that transforms as an invariant under the operations of the crystal point symmetry group, while ↑ (↓) denote the spin functions with projection $S_z = +1\ (-1)$. Close to the band edge the energies of these states are given by

$$H_{v\pm 1/2}(\boldsymbol{k}) = E_v - \frac{\hbar^2\mathbf{k}^2}{2m_v}, \tag{S6}$$

where m_v is the valence band effective mass at the band edge, E_v and $\mathbf{k}$ is restricted to the plane perpendicular to the stacking axis of the 2D perovskite. Here it is assumed, as is confirmed by the DFT calculations in Fig S4, that dispersion in the direction perpendicular to the sheets is negligible, that is, the electronic coupling between individual lead-halide sheets is negligible.

For the electrons in bulk cubic perovskites, the band edge Bloch functions are the 2-fold degenerate states of total angular momentum $J = 1/2$, but with odd orbital parity:

$$u^{c}_{\frac{1}{2},\frac{1}{2}} = \frac{-1}{\sqrt{3}}\{Z\uparrow + (X + i\,Y)\downarrow\}; \qquad u^{c}_{\frac{1}{2},-\frac{1}{2}} = \frac{1}{\sqrt{3}}\{-(X - i\,Y)\uparrow + Z\downarrow\}. \tag{S7}$$

In this expression the symbols X, Y, Z denote orbital functions that transform like *x, y, z* under rotations. For 2D perovskites however, the conduction band Bloch functions take a more complicated form due to the anisotropy of the 2D layer structure. As before, based on the negligible dispersion in the stacking direction, we neglect coupling between lead-halide sheets. Then the Hamiltonian for a single sheet with zero in-plane wave vector consists of the spin-orbit interaction, $H_{LS} = \frac{\Delta_{SO}}{2}\boldsymbol{L}\cdot\boldsymbol{S}$ whose strength is given by Δ_{SO}, the spin-orbit split-off parameter, and the effective crystal field splitting, H_{CF}, due to the confinement in the z direction:

$$H_0 = H_{LS} + H_{CF}\,. \tag{S8}$$

The effective crystal field Hamiltonian is represented in the X, Y, Z orbital basis within a quasi-tetragonal approximation by [24]

$$\widetilde{H}_{CF} = \begin{pmatrix} \frac{\delta}{3} & 0 & 0 \\ 0 & \frac{\delta}{3} & 0 \\ 0 & 0 & -\frac{2}{3}\delta \end{pmatrix}. \tag{S9}$$

The eigenvectors are found by diagonalizing the matrix $\widetilde{H}_{CF} + \widetilde{H}_{LS}$ in Eq. S8. The result is that the $J = \frac{1}{2}, J_z = \pm\frac{1}{2}$ mix with the $J = \frac{3}{2}, J_z = \pm\frac{1}{2}$ states, that is, the projection of total angular momentum on the z axis, J_z, remains a good quantum number. The solution corresponding to the lowest energy conduction band has $J_z = \pm\frac{1}{2}$ Bloch functions given by [23,25–27],

$$u^c_{\frac{1}{2}} = -\left\{\sin\theta\, Z \uparrow + \cos\theta \frac{(X + i\,Y)}{\sqrt{2}} \downarrow\right\}; \qquad u^c_{-\frac{1}{2}} = \left\{-\cos\theta \frac{(X - i\,Y)}{\sqrt{2}} \uparrow + \sin\theta\; Z \downarrow\right\}, \tag{S10}$$

where the phase angle θ determines the mixing of the $J = ½$ and $J = 3/2$ states and is determined by the SOC Δ_{SO} and the crystal field δ: [25–27]

$$\tan 2\theta = \frac{2\sqrt{2}\,\Delta_{SO}}{\Delta_{SO} - 3\delta}, \qquad \theta \leq \frac{\pi}{2}. \tag{S11}$$

For reference, the tetragonal crystal field parameter in a similar PbI_4-based 2D MHP has been previously measured as $\sin\theta = 0.227$ [26], while for $PbBr_4$-based 2D MHPs the measured range is $\sin\theta = 0.2 - 0.32$[27,28] [27,28] Close to the band edge, the energies of these states are given by

$$H_{c\pm 1/2}(\boldsymbol{k}) = E_c + \frac{\hbar^2\mathbf{k}^2}{2m_c}, \tag{S12}$$

where m_c is the conduction band effective mass at the band edge, E_c, and again, $\mathbf{k}$ is restricted to the plane perpendicular to the stacking axis of the 2D perovskite. We will return to the question of the physical origin of the effective crystal field in Section S6 but proceed for the time being with the phenomenological description represented by Eqs. S10-11.

Section S3.1 Dielectric response of free carrier transitions in 2D perovskites

Once the single particle states and their energies are known, the imaginary part of the dielectric function associated with polarization along direction $\hat{u}$, which we denote as $Im\, \epsilon_{uu}(\omega)$, can be determined using the formula [29]

$$Im\, \epsilon_{uu}(\omega) = \frac{4\,\pi^2 e^2}{m_0^2\, \omega^2} \sum_{c,v} \frac{1}{V} \sum_{\boldsymbol{k}} \left|\hat{u} \cdot \boldsymbol{p}_{c,v}(\boldsymbol{k})\right|^2 \, \delta(E_c(\boldsymbol{k}) - E_v(\boldsymbol{k}) - \hbar\omega), \tag{S13}$$

where m_0 and e are the free electron mass and charge; the first sum is taken over the two conduction and two valence bands per layer, indexed respectively by c, v; and $\boldsymbol{p}_{c,v}(\boldsymbol{k})$ is the interband momentum matrix element between conduction band state $c, \boldsymbol{k}$ and valence band state $v, \boldsymbol{k}$, given in terms of the momentum operator $\widetilde{\boldsymbol{p}}$ by

$$\boldsymbol{p}_{c,v}(\boldsymbol{k}) = \langle \psi_{c,\boldsymbol{k}'} | \widetilde{\boldsymbol{p}} | \psi_{v,\boldsymbol{k}} \rangle \cong \langle u_{c,\boldsymbol{k}} | \widetilde{\boldsymbol{p}} | u_{v,\boldsymbol{k}} \rangle \, \delta_{\boldsymbol{k}',\boldsymbol{k}} \,. \tag{S14}$$

Near the band edge, the Bloch functions $u_{n,\boldsymbol{k}}$ can be approximated by the band edge functions u_{n0}. In this approximation, $\boldsymbol{p}_{c,v}(\boldsymbol{k}) \approx \boldsymbol{p}_{c,v}(0)$ and the imaginary part of the dielectric function can be approximated by

$$Im\, \epsilon_{uu}(\omega) \approx \frac{4\,\pi^2 e^2}{m_0^2\, \omega^2} \sum_{c,v} \left|\hat{u} \cdot \boldsymbol{p}_{c,v}(0)\right|^2 \frac{1}{V} \sum_{\boldsymbol{k}} \delta(E_c(\boldsymbol{k}) - E_v(\boldsymbol{k}) - \hbar\omega)\,. \tag{S15}$$

It is convenient to recast this in terms of the total oscillator strength f_u for polarization along direction $\hat{u}$, summed over the four possible transitions c, v associated with a given wave vector $\boldsymbol{k}$, where

$$f_u = \frac{2}{m_0 \hbar\omega} \sum_{c,v} \left|\hat{u} \cdot \boldsymbol{p}_{c,v}(0)\right|^2. \tag{S16}$$

Using this expression, the imaginary part of the dielectric function can be approximated near the band edge by

$$Im\, \epsilon_{uu}(\omega) \approx \frac{2\hbar\,\pi^2 e^2}{m_0\, \omega} \; f_u \; \frac{1}{V} \sum_{\boldsymbol{k}} \delta(E_c(\boldsymbol{k}) - E_v(\boldsymbol{k}) - \hbar\omega)\,. \tag{S17}$$

Within the K.P theory we can evaluate the oscillator strength explicitly. Using Eqs. S5 and S10, the result is can be expressed in terms of the Kane matrix element $P_K = -i\langle S|\tilde{p}_x|X\rangle = -i\langle S|\tilde{p}_y|Y\rangle = -i\langle S|\tilde{p}_z|Z\rangle$ as [23]

$$f_u = \frac{2\, {P_K}^2}{m_0 \hbar\omega} g_u, \tag{S18}$$

where the polarization dependence is given by the dimensionless functions g_u whose values along the x,y, z directions are

$$g_z = 2 \sin^2\theta, \tag{S19}$$

$$g_x = g_y = \cos^2 \theta. \tag{S20}$$

Using Eq S18-S20 in Eq. S17 and noting that the oscillator strength associated with the two in-plane directions x, y are equal ($f_x = f_y$) implies that $\epsilon_{xx}(\omega) = \epsilon_{yy}(\omega)$ in this model, we see that the phase angle θ can be determined from the ratio of the imaginary part of the dielectric function for polarization in the out-of-plane versus the in-plane directions:

$$\frac{Im\,\epsilon_{zz}(\omega)}{Im\,\epsilon_{xx}(\omega)} = \frac{Im\,\epsilon_{zz}(\omega)}{Im\,\epsilon_{yy}(\omega)} = \frac{f_z}{f_x} = 2\tan^2\theta \tag{S21}$$

This identification allows us to estimate the band edge oscillator strength ratio f_z/f_x directly from the DFT calculations of the imaginary part of the dielectric function, shown in Fig. 4d of the main text. In Fig. S7 panel (a) we plot the imaginary part of the dielectric function along the three directions a, b, c calculated as in Fig 4 of the main text, but using DFT-PBE+SOC with a denser (3x15x15) k-grid and a Gaussian broadening function with full-width at half-maximum (FWHM) set to 100 meV. As shown in Fig. 4d of the main text, the near equality of the in-plane dielectric response along the in-plane b and c directions, $\epsilon_{bb}(\omega) \cong \epsilon_{cc}(\omega)$ within 1.2%, is evident in the figure, which justifies the use of the quasi-tetragonal approximation developed above. In Fig. S7 panel (b) we show the ratio $Im\,\epsilon_{\perp}/Im\,\epsilon_{\parallel}$ from the DFT-PBE+SOC calculation shown in Fig S7 panel (a), where $Im\,\epsilon_{\perp}$ corresponds to the out-of-plane crystallographic direction a, and $Im\,\epsilon_{\parallel}$ corresponds to the average of the two in-plane directions $Im\,\epsilon_{bb}\ and\ Im\,\epsilon_{cc}$. The ratio is 7.71% at the band edge, $E_g = 1460$ meV, and increases with increasing energy. At an energy $T_{10} = 120$ meV above the band edge, corresponding to the calculated kinetic energy of the 1S exciton state (see Section 5.2), the ratio increases to 8.68%. Using Eq. S21 these numbers imply $\sin\theta = 0.193$ at the band edge; and an average value $\sin\theta = 0.204$ for the 1S exciton.

In the next section, we use the multiband effective mass theory to show that the ratio of the oscillator strength of the exciton along the extra-ordinary and ordinary directions is also determined by Eq. S21 and can therefore be estimated from the DFT-PBE+SOC calculation of the dielectric response shown in Fig S7.

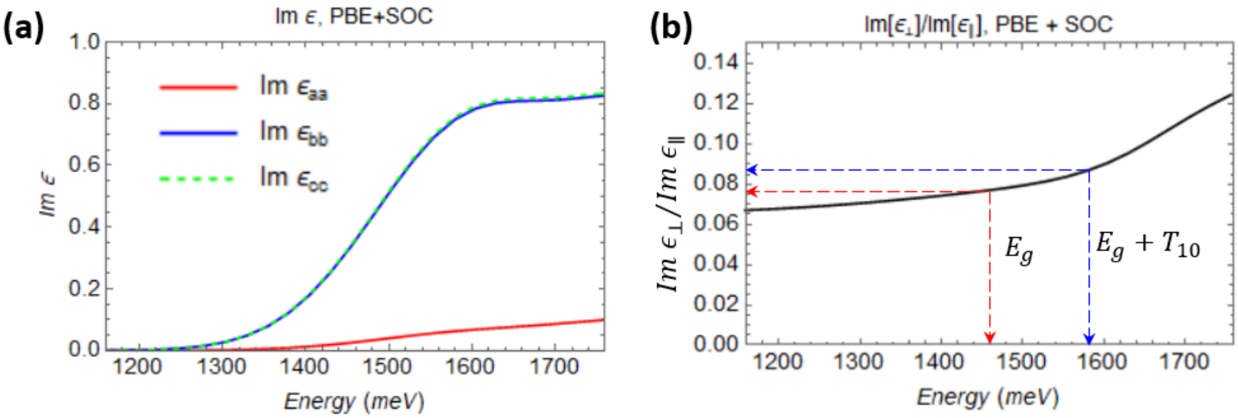

Figure S7. Imaginary part of the dielectric function in PEPI. Panel (a): Imaginary part of the dielectric function $Im\ \epsilon$ along the three crystallographic directions a, b, c calculated using DFT-PBE+SOC and a Gaussian broadening function with FWHM set to 100 meV. The dielectric function along the two in-plane directions b, c are the same within 1.2% over the range plotted. Panel (b): ratio $Im\ \epsilon_\perp / Im\ \epsilon_\parallel$ calculated setting $Im\ \epsilon_\perp = Im\ \epsilon_{aa}$, corresponding to the out-of-plane polarization, and $Im\ \epsilon_\parallel = (Im\ \epsilon_{bb} + Im\ \epsilon_{cc})/2$, corresponding to the average dielectric associated with in-plane polarization. At the bandgap calculated in DFT-PBE+SOC, $E_g = 1460$ meV, marked in red, the ratio $Im\ \epsilon_\perp(\omega)/Im\ \epsilon_\parallel(\omega) = 7.71\%$. At an energy $T_{10} = 120$ meV above the band gap, corresponding to the calculated average kinetic energy of the 1S exciton (see section S5.2), the dielectric anisotropy $Im\ \epsilon_{zz}/Im\ \epsilon_{xx} = 8.68\%$. See text.

Section S4. Effective mass model of excitons in 2D perovskites and their dielectric response.

In the last section we used the K.P method to relate the anisotropic dielectric function calculated in the near band edge region to the properties of the band edge Bloch functions dictated by symmetry. Using the expressions developed we were able to extract crystal field parameters which determine the near band edge anisotropy from the anisotropic dielectric function calculated within DFT. In this section, we use the multiband effective mass theory based on multiband K.P to show that the same symmetry properties of the band edge Bloch functions determine the anisotropic dielectric properties of the exciton as well. In the discussion that follows we retrace the analysis first presented in Refs [23,24] in the context of bulk perovskites and perovskite nanocrystals.

The wave function of an exciton confined in a single 2D MHP layer can be written in the effective mass approximation as a product wave function in the form of a Bloch wave [23],

$$\psi^{ex}_{J_{ze},J_{zh}\boldsymbol{K};nm}(\boldsymbol{r}_e,\boldsymbol{r}_h) = u_{J_{ze}}(\boldsymbol{r}_e)\ u_{J_{zh}}(\boldsymbol{r}_h)\ f_{\boldsymbol{K};nm}(\boldsymbol{r}_e,\boldsymbol{r}_h). \tag{S22}$$

Here, $u_{J_{ze}}$ and $u_{J_{zh}}$, respectively denote the band-edge periodic Bloch functions for the electron and hole, which as we showed above in Eqs. S5 and S10 can be represented in terms of eigenstates of the projection of the total angular momentum in the stacking direction, which we take as z, while the envelope function for the exciton, $f_{n,K}(\boldsymbol{r}_e,\boldsymbol{r}_h)$, describes the motion of the electron and hole within the layer. We take the layer to be normal to the z direction and of thickness d < Λ, where Λ is the spacing between layers and neglect coupling between the layers as justified by the lack of dispersion in the stacking direction evident in the DFT calculations shown in Fig S4. Then, considering the 2D exciton states corresponding to the lowest confined state in the sheet, modelled as a quantum well of thickness d, the exciton envelope function is described by the expression, [29]

$$f_{\boldsymbol{K};nm}\left(\boldsymbol{r}_{\boldsymbol{e}},\boldsymbol{r}_{h}\right)=\frac{1}{\sqrt{S}}e^{i\boldsymbol{K}\cdot\boldsymbol{R}}\frac{2}{d}\cos\frac{\pi z_{e}}{d}\cos\frac{\pi z_{h}}{d}\phi_{nm}(\boldsymbol{r}_{\boldsymbol{e}}-\boldsymbol{r}_{h}). \tag{S23}$$

Here, the envelope function, normalized over the sheet area, S, is specified in terms of the center-of-mass (COM) wave vector $\boldsymbol{K}$ and quantum numbers n, m representing the principle and azimuthal quantum numbers associated with the state of internal relative motion of the electron (e) and hole (h) in the layer. The lowest exciton has quantum numbers $n = 1$ and $m = 0$ and can be considered the 2D analogue of a 1s hydrogenic state. In the absence of dielectric confinement effects, this "ground" exciton level has a relative e/h coordinate wave function given by [30],

$$\phi_{10}(\boldsymbol{r})=\frac{4}{a_x}\frac{1}{\sqrt{2\pi}}e^{-2r/a_x}\,. \tag{S24}$$

In the expression above, a_x is the three-dimensional exciton Bohr radius, given by $a_x = \epsilon\hbar^2/\mu e^2$ where ϵ is the effective dielectric constant that screens the e/h Coulomb interaction [31] and μ is the effective mass given in terms of the electron and hole effective masses m_e and m_h in the plane of the lead-halide sheet by $1/\mu = 1/m_e + 1/m_h$. The energy of the excitons associated with the relative e/h and COM motion is given by,

$$E_{n,m}(\boldsymbol{K}) = E_g + \mathcal{E}_n + \frac{\hbar^2\mathbf{K}^2}{2M}\,, \tag{S25}$$

where E_g is the band gap energy, $\mathcal{E}_n$ are the energy eigenvalues associated with solution of the electron-hole relative motion problem, and the third term represents the kinetic energy of exciton COM motion involving the total exciton effective mass $M = m_e + m_h$.

In addition to the energy associated with electron-hole relative and COM motion given in Eq S25 the exciton also has a fine structure determined by spin-dependent interaction between the electron and hole. The electron-hole exchange interaction can be written in the effective mass approximation as a contact interaction between the electron and hole spins [32]:

$$H_{SR} = \frac{1}{2}C\,\Omega\,[\boldsymbol{I} - \boldsymbol{\sigma}_e.\boldsymbol{\sigma}_h]\,\delta(\boldsymbol{r}_e - \boldsymbol{r}_h)\,, \tag{S26}$$

where $\boldsymbol{\sigma}_e$ and $\boldsymbol{\sigma}_h$ are Pauli operators representing the spin (not the total angular momentum) of the electron and the hole, respectively; $\boldsymbol{r}_e$ and $\boldsymbol{r}_h$ are the e/h position vectors, C is the exchange constant for the material, and Ω is the unit cell volume. In Refs. [23,24], it was shown that averaging the exchange Hamiltonian Eq. S26 over the envelope function portion of Eq S22 results in an effective spin operator for the bulk exciton which acts on the Bloch functions within the total exciton wavefunction, Eq. S22. This effective Hamiltonian can be written,

$$H_{SR} = \frac{1}{2} w \left[\boldsymbol{I} - \boldsymbol{\sigma}_e . \boldsymbol{\sigma}_h \right] . \tag{S27}$$

Here, w is the effective exciton exchange constant, given by $w = C\,\Theta$ where the term Θ is the electron-hole overlap factor, representing the probability that the electron and hole reside in the same unit cell. For the exciton state indexed by it can be written,

$$\Theta_{nm,\boldsymbol{K}} = \Omega \iint_V d^3\boldsymbol{r_e} d^3\boldsymbol{r_h}\, f^*_{nm,K}(\boldsymbol{r}_e, \boldsymbol{r}_h) \delta(\boldsymbol{r}_e - \boldsymbol{r}_h) f_{nm,\boldsymbol{K}}(\boldsymbol{r}_e, \boldsymbol{r}_h). \tag{S28}$$

Evaluating the overlap factor for the ground exciton level ($n = 1$, $m = 0$) in the absence of dielectric confinement effects we find,

$$\Theta_{10,\boldsymbol{K}} = \Omega \frac{3}{2d} \frac{8}{\pi a_x^2}. \tag{S29}$$

For reference the value of the effective exciton exchange constant determined from measurements of the exciton fine structure in a related PbI$_4$-based 2D MHP is $w = 12$meV [27]. To develop a matrix representation for the exciton exchange Hamiltonian, Eq. S27, we use the electron hole pair basis,

$$P_1 = u^e_{1/2} u^{eh}_{1/2};\ P_2 = u^e_{1/2} u^h_{-1/2};\ P_3 = u^e_{-1/2} u^h_{1/2};\ \text{and } P_4 = u^e_{-1/2} u^h_{-1/2}\ , \tag{S30}$$

where $u^{e(h)}_{\pm 1/2}$ are the band edge Bloch functions for the conduction and valence bands defined in Eqs. S5 and S10. We find the exchange Hamiltonian has the following representation:

$$\widetilde{H}_{Pair} = w \begin{pmatrix} \cos^2\theta & 0 & 0 & 0 \\ 0 & \sin^2\theta & \sin^2\theta & 0 \\ 0 & \sin^2\theta & \sin^2\theta & 0 \\ 0 & 0 & 0 & \cos^2\theta \end{pmatrix} \tag{S31}$$

It is convenient to diagonalize this Hamiltonian with the transformation [33],

$$\widetilde{H}_{XYZ} = \widetilde{M}_2{}^{\dagger} \widetilde{M}_1{}^{\dagger} \widetilde{H}_{Pair}\ \widetilde{M}_1 \widetilde{M}_2\ ,$$

where the unitary transformation matrices $\widetilde{M}_1,\ \widetilde{M}_2$ are given by,

$$\widetilde{M}_1 = \begin{pmatrix} 0 & 1 & 0 & 0 \\ \frac{-1}{\sqrt{2}} & 0 & \frac{1}{\sqrt{2}} & 0 \\ \frac{1}{\sqrt{2}} & 0 & \frac{1}{\sqrt{2}} & 0 \\ 0 & 0 & 0 & 1 \end{pmatrix} \quad \text{and} \quad \widetilde{M}_2 = \begin{pmatrix} 1 & 0 & 0 & 0 \\ 0 & \frac{-1}{\sqrt{2}} & \frac{i}{\sqrt{2}} & 0 \\ 0 & 0 & 0 & 1 \\ 0 & \frac{1}{\sqrt{2}} & \frac{i}{\sqrt{2}} & 0 \end{pmatrix}$$

The first transformation ($\widetilde{M}_1$) transforms the Hamiltonian to a basis of total angular momentum $F = J_e + J_h$, taken in the order, $|F, F_z> = |0,0>, |1,+1>, |1,0>, |1,-1>$, while the second diagonalizes the Hamiltonian in a basis of exciton states, taken in the order $|D>, |X>, |Y>, |Z>$, whose transition dipoles to the crystal ground state respectively vanish (D) or are aligned along the symmetry directions x, y, z. In this basis the exchange Hamiltonian is diagonal with exciton eigen-energies given by,

$$E_X = E_Y = w \cos^2\theta, \quad \text{(S32)}$$
$$E_Z = 2\, w \sin^2\theta,$$
$$E_D = 0 \; .$$

It is straightforward to determine the oscillator strength of each exciton state $|X_i>$, where X_i denotes D, X, Y or Z. The transition dipole matrix elements (DME) are found as the matrix element of the momentum operator, $\hat{\boldsymbol{p}}$, between a given exciton total wave function, $\psi_{X_i}^{ex} = \Phi_{X_i} f_{nm;\boldsymbol{K}}(\boldsymbol{r_e}, \boldsymbol{r_h})$, which is written as the product of the Bloch function eigenstate, $\Phi_{X_i} = \sum_{i=1}^{4} c_i P_i$ and the envelop function $f_{nm;\boldsymbol{K}}(\boldsymbol{r_e}, \boldsymbol{r_h})$, and the crystal ground state G, which is represented by $\delta(\boldsymbol{r_e} - \boldsymbol{r_h})$. Denoting the exciton DME for exciton state X_i as P_{X_i} and computing the oscillator strength in the usual way as $f_{X_i}{}^{exc} = 2\, P_{X_i}{}^2 / (m_0 \hbar\omega)$ the result is [23,24],

$$f_X{}^{exc} = f_Y{}^{exc} = \frac{2\, P_K{}^2}{m_0 \hbar\omega}\; \mathcal{K}^2 \cos^2\theta, \quad \text{(S33)}$$
$$f_Z{}^{exc} = \frac{2\, P_K{}^2}{m_0 \hbar\omega}\; \mathcal{K}^2\; 2\sin^2\theta,$$
$$f_D{}^{exc} = 0 \; ,$$

Here, P_K is the Kane momentum matrix element as before while the overlap factor $\mathcal{K}$ is given by,

$$\mathcal{K} = \int_V f_{n,m;\boldsymbol{K}}(r, r) dV, \quad \text{(S34)}$$

Evaluating Eq. S34 for the ground exciton relative motion state $n = 1, m = 0$, and using the definition of the Kane energy, $E_p = 2 P_K{}^2 / m_0$, the oscillator strength per unit area for the exciton in a single lead-halide sheet of area S is,

$$\frac{f_{X_i}{}^{exc}}{S} = \frac{E_p}{\hbar\omega}\, |\varphi_{10}(0)|^2\, g_{X_i}. \quad \text{(S35)}$$

In this expression, the term g_{X_i} reflects the anisotropy of the 2D MHP structure and is given in Eq. S19-S20, namely, $g_Z = 2\sin^2\theta$ while $g_X = g_Y = \cos^2\theta$. This makes intuitive sense: The anisotropy of the exciton oscillator strength directly reflects the anisotropy of the band-edge free carrier transitions, which is determined by the crystal field phase factor θ. Modelling the 2D MHP crystal with sheets separated by spacing Λ, the oscillator strength per unit volume is then [34],

$$\frac{f_{X_i}{}^{exc}}{V} = \frac{2\, P_K{}^2}{m_0 \hbar\omega} \frac{|\varphi_{10}(0)|^2}{\Lambda}\, g_{X_i} \quad \text{(S36)}$$

Using this expression we can now describe the polarization dependent intrinsic dielectric response of the exciton X_i [35]:

$$\epsilon_{X_i}(E) = \epsilon_\infty \left\{ 1 + \frac{\hbar\omega_{LT,X_i}}{\left(E_{X_i} - E\right) - i\left(\frac{\Gamma_{X_i}}{2}\right)} \right\}. \tag{S37}$$

This expression represents the dielectric response of the excitons sitting on a non-resonant background dielectric ϵ_∞ . In the brackets, Γ_{X_i} is the full-width at half maximum of the exciton resonance, reflecting the exciton broadening, and polarization dependence enters through the coupling parameter $\hbar\omega_{LT,X_i}$, known as the longitudinal (L) - transverse (T) exciton splitting, which is proportional to the exciton oscillator strength per unit volume: [30],

$$\hbar\omega_{LT,X_i} = \frac{e^2\hbar^2}{2\epsilon_\infty m_0 \hbar\omega} \frac{f_{X_i}{}^{exc}}{V}. \tag{S38}$$

Inspection of Eqs. S36-S38 reveals that the ratio of the polarization dependent oscillator strength of the exciton transitions extracted from analysis of the dielectric response is,

$$\frac{f_z{}^{exc}}{f_x{}^{exc}} = 2\tan^2\theta. \tag{S39}$$

This result is the same as was derived for the free carrier transitions near the band edge, Eq. S21. Referring to Fig S7, the DFT-PBE+SOC calculation shows that z:x oscillator strength ratio has a weak energy dependence above the band gap. In this case the appropriate ratio for the exciton corresponds to that at the energy $E_g + T_{10}$, where T_{10} is the kinetic energy associated with internal electron-hole motion within the 1S exciton level. In Section 6 we calculate the exciton binding energy for PEPI using the experimental reduced effective mass ($\mu = 0.087$, Ref [21]) and estimate $T_{10,exp} = 160$meV. Correcting the kinetic energy for the ratio of the experimental reduced effective mass to the effective mass determined from the DFT-PBE+SOC band structure ($\mu = 0.116$, see **Table S3**), we find $T_{10} = 120$ meV.The corresponding estimate of the ratio $f_z{}^{exc}/f_x{}^{exc} \sim 8.7\%$ on the basis of the DFT-PBE+SOC calculation shown in Fig S7.

Section S5. Effect of dielectric discontinuity on exciton optical response and binding energy.

In sections S2 and S3 we analyzed the anisotropy of the intrinsic dielectric response of the near-band-edge free carrier transitions and of the excitons in 2D PEPI and showed how the intrinsic excitonic polarization anisotropy can be connected to DFT calculations of the dielectric function near the band edge. A key element missing from the analysis so far is the fact that the excitons are embedded in a *dielectric superlattice*: That is, excitons are confined to the 2D lead-halide layers with a relatively high background dielectric constant (relative dielectric ranging from 4-6), which is surrounded by organic layers with a lower dielectric (with relative dielectric in the range 2-3); moreover this dielectric structure is periodic in the direction normal to the layers.

The resulting anisotropic dielectric environment has significant implications to both the optical response and the exciton binding energy. In the first case, the anisotropic dielectric environment causes an enhancement of the polarization anisotropy above that expected purely on the basis of the anisotropy of the electronic states owing to the distinct boundary conditions associated with electric field vectors parallel versus perpendicular to a planar dielectric interface, as shown recently by DeCresent *et al.* in Ref [36]. In the second case, the electron-hole interaction responsible for the exciton binding must include the effects of image charges owing to the dielectric discontinuity. The resulting interaction of the electron (hole) with the image charges of the hole (electron) causes a significant increase in the electron binding energy relative to the situation in traditional III-V semiconductor multi-quantum well systems which lack significant dielectric discontinuity between the well and barrier regions.

In this section we first employ the analysis of DeCresent *et al*. to infer the intrinsic dielectric constants of the inorganic well and organic barrier layers of 2D PEPI from the spectroscopic ellipsometry measurements discussed in the main text. Then, to confirm that the inferred dielectric parameters are reasonable, we use the theory developed by Guseinov in Ref. [37] for exciton binding in dielectric multilayers to calculate the exciton binding energy. Using measured effective masses [21] and the inferred dielectric parameters we find excellent agreement with the exciton binding energy recently measured in 2D PEPI [21].

Section S5.1 Effect of dielectric discontinuity on exciton optical response

The analysis of DeCresent *et al.* in Ref [36] begins with the observation that at a planar dielectric interface the electric field components parallel versus perpendicular to the interface are subject to distinct boundary matching conditions: Denoting the dielectric of the inorganic well as ϵ and the organic barrier as ϵ_b, the boundary matching conditions from the left (-) t the right (+) side of an interface are,

$$E_{\parallel}^{-} = E_{\parallel}^{+}, \qquad \text{(S40)}$$

$$\epsilon_{\perp} E_{\perp}^{-} = \epsilon_{b,\perp} E_{\perp}^{+} \ .$$

As a consequence of these matching conditions, excitons in the inorganic layers interact with light polarized parallel to the interface without any depolarization effect, while the interaction of excitons with light polarized perpendicular to the interface is attenuated by a depolarization factor; DeCresent *et al.* showed that the resulting *effective* oscillator strength for the exciton out of plane is [36]

$$f_z^{\,eff} = \left(\frac{\bar{\epsilon}_{\perp}}{\epsilon_{\perp}}\right)^2 f_z^{\,exc}, \qquad \text{(S41)}$$

where $\bar{\epsilon}_{\perp}$ denotes the effective out-of-plane permittivity of the superlattice, and is given in terms of the intrinsic out-of-plane permittivities of the well ($\epsilon_{\perp}$) and barrier ($\epsilon_{b,\perp}$) layers and volume fill fraction, f, of the high-dielectric well layer by,

$$\bar{\epsilon}_{\perp} = \frac{1}{f/_{\epsilon_{\perp}} + (1-f)/_{\epsilon_{\mathrm{b},\perp}}} \quad . \tag{S42}$$

Notably, the effective out-of-plane permittivity $\bar{\epsilon}_{\perp}$ is what is measured in polarization-resolved spectroscopic ellipsometry. Consequently, with information about the fill fraction, f, and the organic dielectric permittivity $\epsilon_{\mathrm{b},\perp}$ Eq. S42 can be used to estimate the intrinsic dielectric permittivity of the inorganic later. Using the lead-halide and organic layer thicknesses determined for PEPI in Ref [7] we estimate $f = 0.39$, taking the refractive index of the organic layer to be isotropic with value $n = 1.6$ [36] and using the measured $n_e = 1.8$ at the exciton line from Fig 2(c) of the main text, and using $\bar{\epsilon}_{\perp} = n_e{}^2$, we estimate the intrinsic dielectric permittivity of the inorganic well layer to be $\epsilon_{\perp} = 5.4$. Using these values we estimate the correction factor relating the measured, effective, out-of-plane to in-plane oscillator strength ratio of the exciton, to the intrinsic oscillator strength ratio, as $(\epsilon_{\perp}/\bar{\epsilon}_{\perp})^2$:

$$\left(\frac{f_z{}^{exc}}{f_x{}^{exc}}\right)^{intrinsic} = \left(\frac{\epsilon_{\perp}}{\bar{\epsilon}_{\perp}}\right)^2 \left(\frac{f_z{}^{exc}}{f_x{}^{exc}}\right)^{measured} . \tag{S43}$$

From the measured value $(f_z{}^{exc}/f_x{}^{exc})^{meas} \sim 0.059$ for cleaved single crystals (see Table 1) we estimate the intrinsic ratio $(f_z{}^{exc}/f_x{}^{exc})^{intrinsic} \sim 0.166$. These values are summarized in **Table S4** along with the estimate of the intrinsic exciton oscillator strength ratio derived from the DFT-PBE+SOC calculations shown in Fig S7. The DFT based estimate, at 0.087, is about 48% lower than the intrinsic ratio inferred from the measured values by applying the classical dielectric anisotropy model. This discrepancy may be due the fact that the DFT methods applied here are restricted to single-particle band-to-band transitions and do not account for excitonic effects, which are modelled within a simple effective mass approximation, or alternately due to a failure of the classical dielectric interface model employed to estimate the local field screening corrections, which assumes abrupt dielectric interfaces. As an independent check of the reasonableness of the intrinsic dielectric parameters recovered using the dielectric anisotropy model, we made a calculation of the exciton binding energy using the recovered dielectric parameters, which is described next.

Table S4. Intrinsic dielectric properties and oscillator strength ratio

Parameter	**Value**	**Source**
Inorganic fill fraction f	0.39	Ref. [7]
Organic layer relative dielectric permittivity $\epsilon_{b,\perp}$	2.56	Ref. [36]
Extraordinary index n_e at exciton line	1.8	This work, Fig 2(c)
Inorganic layer intrinsic dielectric permittivity $\epsilon_\perp$	5.4	This work Eq. S42
Correction factor, $\left(\frac{\epsilon_\perp}{\bar{\epsilon}_\perp}\right)^2$	2.81	This work, Eq. S43
Measured exciton anisotropy: $(f_z{}^{exc}/f_x{}^{exc})^{meas}$	0.059	This work, Table 1, cleaved crystal sample
Estimated intrinsic exciton anisotropy from measurements and dielectric anisotropy model: $(f_z{}^{exc}/f_x{}^{exc})^{intrinsic}$	0.166	This work, Eq. S43
Estimated intrinsic exciton anisotropy from DFT-PBE+SOC calculations: $(f_z{}^{exc}/f_x{}^{exc})^{intrinsic}$	0.087	This work, Fig S7

Section S5.2 Effect of dielectric discontinuity on exciton binding energy

It is well known that in the presence of significant dielectric discontinuities between well and barrier layers, such as occur in 2D MHPs such as PEPI, the influence of image charges must be accounted for in calculating the exciton binding energy [8,37–41]. The effects were first modelled by Rytova [38] and Keldysh [39] within a 3-layer slab dielectric model. That is, Rytova and Keldysh solved for the potential of a point charge located within a dielectric well surrounded by semi-infinite dielectric barrier layers. The Rytova/Keldysh solution was further restricted to the limiting approximation that the electron-hole separation is much larger than the film thickness [38,39]. In 1988 Hanamura applied a real-space image charge potential for the 3-layer slab allowing the latter approximation to be relaxed [40]; the Hanamura method was applied in 1992 by Hong and co-workers [8] in a variational calculation of the exciton binding energy in 2D MHPs including PEPI using trial wavefunctions of the form given above in Eq. S23, *i.e.* assuming infinite barriers at the well/barrier interface [8], which is a reasonable approximation given the dissimilarity of the periodic Bloch functions between the well and barrier layers [42]. However, the Hanamura/Hong method significantly overestimates the image charge effect in dielectric superlattices where the low dielectric layer thickness is comparable to the high dielectric well thickness: The magnitudes of higher order image charges are overestimated when the high dielectric of adjacent wells in the superlattice is neglected. The 3- layer slab approximation was relaxed in the calculation by Guseinov in 1984 [37] who wrote an exact solution for the electron-hole interaction in a dielectric superlattice using k-space methods; the Guseinov potential was adopted by Muljarov *et al.* who applied it to 2D MHPs including PEPI using a *finite* well/barrier heterointerface model [41]. The latter assumption, as noted in Ref. [42], is questionable due to the chemical dissimilarity of the well/barrier constituents; moreover this assumption in conjunction with the abrupt dielectric discontinuity creates singularities in the Coulomb self-energy which necessitates the introduction of an ad-hoc interface transitional layer as a fitting parameter [41].

To avoid this ad-hoc procedure, we apply the exact solution for the electron-hole interaction in a dielectric superlattice derived by Guseinov [37] and calculate the exciton binding energy using a variational procedure using an exciton ansatz function of the form given in Eq. S23.

Section S5.2.1 Guseinov potential

Guseinov, in Ref. [37], solved Poisson's equation using Fourier analysis to determine the electrostatic potential at a position (z, ρ) in cylindrical coordinates, given a source located at (ρ, z_s) within a system comprising a dielectric superlattice normal to the z direction. The superlattice is comprised of well layers of thickness d with relative dielectric ϵ alternating with barrier layers of thickness b and dielectric ϵ_b. For the special case that the source and observation points reside in the same well layer, taken to be located $-d < z;\ zs < 0$, the solution has the form,

$$\begin{aligned} V(z, z_s, \rho) &= \frac{1}{(2\pi)^2}\int d^2\, k e^{-k\rho}\tilde{V}(z, z_s, k) \\ &= \frac{1}{2\pi}\int_0^\infty k\, dk J_0\left(\frac{\rho x}{b}\right)\tilde{V}(z, z_s, k) \end{aligned} \tag{S44}$$

where the Fourier transform of the potential, $\tilde{V}$, is given in SI units by,

$$\tilde{V}(z, z_s, k) = \frac{e}{4\pi\epsilon_0\epsilon_b k}\tilde{\Phi}(z, z_s, k)\,; \tag{S45}$$

The dimensionless FT function $\tilde{\Phi}$ is given by,

$$\begin{aligned}\widetilde{\Phi}(z_e, z_h, k) = {} & \frac{\pi}{\sinh[k_0]} \frac{1}{(\alpha \sinh[k(b+d)] + \beta \sinh[k(b-d)])} \\ & \times \{2\eta \cosh[k_0] \cosh[k(z_> - z_<)]\, (\alpha \cosh[k(b+d)] - \beta \cosh[k(b-d)]) \\ & - 2\,\eta \sinh[k_0] \sinh[k(z_> - z_<)]\, (\alpha \sinh[k(b+d)] + \beta \sinh[k(b-d)]) \\ & - 2\cosh[k(z_> - z_<)](\alpha^2 + \beta^2 - 2\,\alpha\,\beta \cosh[k\,b]^2) \\ & + (\alpha - \beta)^2 \cosh[k(2d + z_> + z_<)] \\ & - 2\,\eta \cosh[k_0](\alpha \cosh[k(z_> + z_< + d - b)] \\ & - \beta \cosh[k(z_> + z_< + d + b)]) \\ & + \cosh[k(z_> + z_<)]\big((\alpha^2 + \beta^2)\cosh[2k\,b] - 2\alpha\,\beta\big) \\ & - \eta \sinh[k(z_> + z_<)]\sinh[2k\,b]\}\,. \end{aligned} \tag*{S46)}$$

In this expression, $z_>$ ($z_<$) is the greater (lesser) of z, z_s, k is the component of the wave-vector in the z direction, and the other term are defined by,

$$\eta = \epsilon_b/\epsilon; \qquad \alpha = \frac{1+\eta}{2}\,; \qquad \beta = \frac{1-\eta}{2}$$

$$k_0 = \cosh^{-1}\left(\frac{2\alpha^2}{2\alpha - 1}\sinh(kb)\sinh(kd) + \cosh\big(k(b-d)\big)\right) \tag{S47}$$

Adopting a variational wavefunction for the lowest energy exciton of the form Eq S23, but taking the quasi-2D exciton radius a as a variational parameter,

$$\psi_{1,0}(z_e, z_h, \boldsymbol{\rho}) = \frac{2}{d}\cos\frac{\pi(z_e + d/2)}{d}\cos\frac{\pi(z_h + d/2)}{d}\frac{4}{a}\frac{1}{\sqrt{2\pi}}e^{-2\rho/a}\ , \tag{S48}$$

we compute the energy for the 1S exciton state (n=1, m=0, where quantum numbers n, m represent the principle and azimuthal quantum numbers associated with the state of internal relative motion) as,

$$\mathrm{E}_{1,0}(\mathrm{a}) = \int_{-\mathrm{d}}^{0}\int_{-\mathrm{d}}^{0}\int_{0}^{2\pi}\int_{0}^{\infty} \rho\ \mathrm{d}\rho\, \mathrm{d}\theta\, \mathrm{d}z_{\mathrm{e}}\mathrm{d}z_{\mathrm{h}}\ \psi_{10}^{*}(\rho; \mathrm{a})\, \widehat{H}_{rel}\ \psi_{10}(\rho; \mathrm{a})\ . \tag{S49}$$

Here, the effective Hamiltonian for the electron/hole relative motion given by,

$$\widehat{H}_{\mathrm{REL}} = -\frac{\hbar^2\nabla_\rho^2}{2\mu} - eV(z_e, z_h, \rho), \tag{S50}$$

where the interaction potential V is given by Eq S44. The optimum value of the variational parameter is the value that minimizes the energy: $a_{10} = a_{min}$. The kinetic energy terms evaluate to [30],

$$\mathrm{T}_{1,0} = \frac{\hbar^2}{2\mu}\frac{4}{a_{10}^2}\ , \tag{S51}$$

where μ is the reduced effective mass of the exciton. The same procedure can be used to calculate higher exciton states. For example, the 2S (n=2, m=0) exciton state is calculated using the ansatz function,

$$\psi_{2,0}(z_e, z_h, \boldsymbol{\rho}) = \frac{2}{d}\cos\frac{\pi(z_e + d/2)}{d}\cos\frac{\pi(z_h + d/2)}{d}\frac{1}{\sqrt{2\pi}}\frac{4\mathrm{e}^{-\frac{2\rho}{3a}}\left(1 - \frac{4\rho}{3a}\right)}{3\sqrt{3}a}, \tag{S52}$$

In **Table S5** we summarize the calculated results as well as the parameters used in the calculation. The dielectric parameters used are taken from **Table S4** and represent our analysis of the ellipsometry data at the exciton line as described in Section S5.1, while the reduced effective mass of the exciton is taken from the magneto-reflectivity measurements in the recent work by Dyksik *et al.*, Ref [21]. Referring to **Table S3**, the band edge reduced effective mass calculated from the DFT-HSE06+SOC band structure is $\mu = 0.116$ averaged over the in-plane k-space directions, in reasonable agreement with the experimental value. Using the experimental effective mass and dielectric parameters, the exciton binding energy calculated using Eq. S49 is $\mathrm{E}_{1,0}(a_{10}) = -259$ meV relative to the band edge, in excellent agreement with the experimental value -265 meV from Ref. [21]. From the optimum quasi-2D exciton radius a_{10} we estimate the diamagnetic shift coefficient σ =1.03 μeV/T^2 in comparison with the reported value σ =0.43 μeV/T^2 from Ref. [21]. The discrepancy between the calculated and experimentally reported value of the diamagnetic shift coefficient is likely related to the small diamagnetic shift relative to the exciton linewidth (~ 1.5meV over 60T in comparison with a ~10 meV PL linewidth). In **Table S5** we also show the result of a variational calculation of the 2S (n=1, m=0) exciton binding energy, $\mathrm{E}_{2,0}(a_{20}) = -38$ meV, since the value $\mathrm{E}_{1,0} - \mathrm{E}_{2,0} = -221$ meV represents an approximate lower bound on experimental determination of the exciton binding energy [43]. It is also noteworthy that the exciton binding energy calculated within the 3-layer slab approximation of Hanamura/Hong [8,40] is 314 meV using the parameters summarized in **Table S5**– significantly larger than obtained with the exact Guseinov multilayer potential employed here.

Table S5. Summary of parameters used in exciton binding energy calculation and calculated results for the 1S and 2S exciton radius and binding energy. Also listed for comparison is the measured 1S exciton binding energy from Ref [15].

Parameter	**Value**	**Source**
Inorganic well thickness, d	0.644nm	Ref. [7]
Organic barrier layer thickness, b	1.024nm	Ref. [7]
Organic layer relative dielectric permittivity ϵ_b	2.56	Ref. [36]
Inorganic layer intrinsic dielectric permittivity ϵ	5.4	This work, **Table S*3***
Exciton reduced effective mass μ	0.087	Ref. [21]
Calculated 1S exciton binding energy, $-E_{1,0}$ 2D exciton radius, a_{10}	259 meV $a_{10} = 3.3$nm	This work
Measured 1S exciton binding energy	265 meV	Ref. [21]
Calculated 2S exciton binding energy, $-E_{2,0}$ 2D exciton radius, a_{20}	38 meV $a_{20} = 2.2$nm	This work

Section S6: Origin of the effective crystal field: Quantum well mixing

In Section S3. Details of K.P model for free carriers in 2D perovskites we described the modification of the conduction band zone-center Bloch functions in terms of a phenomenological effective crystal field model. Here we show that the effective crystal field originates from the quantum confinement effect associated with strong confinement in the direction perpendicular to the lead-halide inorganic layers, following the analysis by Sercel and co-workers, first presented in Ref. [44] in analyzing the effect of quantum-well mixing on the conduction band Bloch functions in $CsPbBr_3$ nanoplatelets.

The conduction bands of perovskite semiconductors can be described using the 6-band Luttinger Hamiltonian [45]. In a basis of Bloch functions $|J, J_z\rangle$ written as eigenstates of angular momentum, J, and its projection along the z axis, J_z, written in the order, $|3/2, 3/2\rangle |3/2, -1/2\rangle, |1/2, -1/2\rangle$; $|3/2, -3/2\rangle, |3/2, +1/2\rangle, |1/2, 1/2\rangle$, the Luttinger Hamiltonian has the form,

$$\tilde{H} = \tilde{H}_1 + \tilde{H}_2 \ . \tag{S53}$$

The first term, $\tilde{H}_1$, is isotropic and is given by,

$$\tilde{H}_1 = \frac{1}{2m_0}\gamma_1 \mathbf{p}^2\, \tilde{1}, \tag{S54}$$

where $\tilde{1}$ represents the 6x6 identity matrix, m_0 is the free electron mass, γ_1 is the isotropic Luttinger parameter, and $\mathbf{p} = \hbar\mathbf{k}$. The second term, $\widetilde{H}_2$, can be written, using $T \equiv \gamma_2/2m_0\left(p_x^2 + p_y^2 - 2p_z^2\right)$ and $\mathrm{W}_\pm \equiv \gamma_2/2m_0\left(p_x^2 - p_y^2\right) \pm 2i\gamma_3 p_x p_y$, and $p_\pm \equiv p_x \pm i\, y$, where γ_2 and γ_3 are the second and third Luttinger parameters, as,

$$\widetilde{H}_2 = \begin{pmatrix} \Delta_{SO} + T & -\sqrt{3}W_- & \sqrt{6}W_- & 0 & \frac{-2\sqrt{3}\gamma_3}{2m_0}p_-p_z & \frac{\sqrt{6}\gamma_3}{2m_0}p_-p_z \\ -\sqrt{3}W_+ & \Delta_{SO} - T & -\sqrt{2}T & \frac{2\sqrt{3}\gamma_3}{2m_0}p_-p_z & 0 & \frac{-3\sqrt{2}\gamma_3}{2m_0}p_+p_z \\ \sqrt{6}W_+ & -\sqrt{2}T & 0 & \frac{\sqrt{6}\gamma_3}{2m_0}p_-p_z & \frac{-3\sqrt{2}\gamma_3}{2m_0}p_+p_z & 0 \\ 0 & \frac{2\sqrt{3}\gamma_3}{2m_0}p_+p_z & \frac{\sqrt{6}\gamma_3}{2m_0}p_+p_z & \Delta_{SO} + T & -\sqrt{3}W_+ & -\sqrt{6}W_+ \\ \frac{-2\sqrt{3}\gamma_3}{2m_0}p_+p_z & 0 & \frac{-3\sqrt{2}\gamma_3}{2m_0}p_-p_z & -\sqrt{3}W_- & \Delta_{SO} - T & \sqrt{2}T \\ \frac{\sqrt{6}\gamma_3}{2m_0}p_+p_z & \frac{-3\sqrt{2}\gamma_3}{2m_0}p_-p_z & 0 & -\sqrt{6}W_- & \sqrt{2}T & 0 \end{pmatrix}, \tag{S55}$$

where Δ_{SO} is the spin orbit coupling split-off parameter separating the J=3/2 and J=1/2 states at zone center. Since the matrix $\widetilde{H}_1$ is isotropic it does not affect Bloch function mixing. We focus our attention on the second term, $\widetilde{H}_2$, which mixes the J=3/2 upper bands with the lower spin-orbit split-off band with *J*=1/2, $J_z = \pm 1/2$, which comprises the frontier conduction band. In particular we are interested in the conduction bands in a perovskite slab of thickness d and lateral area S assumed large, and centered at the coordinate at $z = 0$. We adopt a quantum well model as suggested by ab initio studies on 2D HOIPs [17]. Employing the effective mass approximation for the quantum confinement in the z direction and considering only the lowest conduction band electron sub-band, the requirement that the wave function vanishes at the slab surfaces at $z = \pm d/2$ constrains the eigenstates to have the form [44],

$$\psi_{\boldsymbol{k}}(\boldsymbol{r}) = \sqrt{\frac{2}{d}}\cos\frac{\pi z}{d}\,\frac{e^{i(k_x x + k_y y)}}{\sqrt{S}}\quad\sum_{J,J_z} A_{J,J_z}\,|J,J_z\rangle\,, \tag{S56}$$

where A_{J,J_z} are expansion coefficients and $|J,J_z\rangle$ are the full set of zone-center Bloch functions with J = 3/2 and J =1/2. This expression indicates a change of basis from the Bloch function basis $|J,J_z\rangle$ to the quantum well basis $|C\rangle|J,J_z\rangle$, where $\langle z|C\rangle = \sqrt{\frac{2}{d}}\cos\frac{\pi z}{d}$. We transform to this basis using the transformation $\widetilde{H}_2^C = \int_{-d/2}^{d/2} dz\, C(z)\widetilde{H}_2\, C(z)$. The effective Hamiltonian can then be written as,

$$\widetilde{H}_2^C = \begin{pmatrix} \Delta_{SO} + T^C & -\sqrt{3}W_-^C & \sqrt{6}W_-^C & 0 & 0 & 0 \\ -\sqrt{3}W_+^C & \Delta_{SO} - T^C & -\sqrt{2}T^C & 0 & 0 & 0 \\ \sqrt{6}W_+^C & -\sqrt{2}T^C & 0 & 0 & 0 & 0 \\ 0 & 0 & 0 & \Delta_{SO} + T^C & -\sqrt{3}W_+^C & -\sqrt{6}W_+^C \\ 0 & 0 & 0 & -\sqrt{3}W_-^C & \Delta_{SO} - T^C & \sqrt{2}T^C \\ 0 & 0 & 0 & -\sqrt{6}W_-^C & \sqrt{2}T^C & 0 \end{pmatrix}, \tag{S57}$$

where Δ_{SO} is the spin orbit coupling split-off parameter, and,

$$T^C \equiv \frac{\hbar^2}{2m_0}\gamma_2\left(k_x^2 + k_y^2 - 2\left(\frac{\pi}{d}\right)^2\right) ,$$

$$\mathrm{W}_\pm^C \equiv \frac{\hbar^2}{2m_0}\gamma_2\left(k_x^2 - k_y^2\right) \pm 2i\gamma_3 k_x k_y \;\; .$$

The transformation leading to Eq. S57 yields the result that all linear order terms involving p_z vanish, so that $\widetilde{H}_2^C$ decouples into two 3x3 matrices. Additionally, $\widetilde{H}_2^C$ can be separated into a k-independent piece and a k-dependent piece as follows:

$$\widetilde{H}_2^C = \widetilde{H}_2^C(0) + \widetilde{H}_2^C(\boldsymbol{k}) \;. \tag{S58}$$

Notably, the band edge positions are given solely by the k-independent term $\widetilde{H}_2^C(0)$. We re-cast this in the following form:

$$\widetilde{H}_2^C(0) = \begin{pmatrix} \widetilde{H}_C^+ & \tilde{0} \\ \tilde{0} & \widetilde{H}_C^+ \end{pmatrix}, \tag{S59}$$

where $\tilde{0}$ is a 3x3 matrix of zeroes, and the sub-matrices on the diagonal are given by [44],

$$\widetilde{H}_C^\pm = \begin{array}{c} \begin{array}{ccc} \left|\frac{3}{2},\pm\frac{3}{2}\right\rangle & \left|\frac{3}{2},\mp\frac{1}{2}\right\rangle & \left|\frac{1}{2},\mp\frac{3}{2}\right\rangle \end{array} \\ \begin{pmatrix} \Delta_{SO} + \frac{\delta}{3} & 0 & 0 \\ 0 & \Delta_{SO} - \frac{\delta}{3} & \mp\frac{\sqrt{2}}{3}\delta \\ 0 & \mp\frac{\sqrt{2}}{3}\delta & 0 \end{pmatrix} \end{array}, \tag{S60}$$

where the basis functions are given above the matrix for clarity. Diagonalization of each sub-matrix $\widetilde{H}_C^\pm$ yields the band edge energies for the upper heavy electron (he) and light-electron (le) band and the lower conduction band:

$$E_{\pm 1/2}^{he} = \Delta_{SO} - \frac{\delta}{3}; \tag{S61}$$

$$E_{\pm 1/2}^{le} = \frac{1}{6}\left(3\Delta_{SO} - \delta + \sqrt{9\Delta_{SO}{}^2 - 6\delta\Delta_{SO} + 9\delta^2}\right); \tag{S62}$$

$$E_{\pm 1/2}^{c} = \frac{1}{6}\left(3\Delta_{SO} - \delta - \sqrt{9\Delta_{SO}{}^2 - 6\delta\Delta_{SO} + 9\delta^2}\right). \tag{S63}$$

The eigenvectors corresponding to the lowest conduction band, Eq. S63, correspond to the conduction band Bloch functions given in Eqs. S10-11. This is the key result: The parameter δ is here identified as the effective crystal field introduced phenomenologically in Section 2.3. It is given by [44],

$$\delta = -\,6\frac{\hbar^2}{2m_0}\gamma_2\left(\frac{\pi}{d}\right)^2 . \tag{S64}$$

By virtue of the quantum well mixing effect the effective crystal field is negative for positive γ_2. We can estimate its magnitude given the thickness of the inorganic layer, d, and the value of the Luttinger parameter γ_2, which can be estimated from the bandgap, E_g, and the Kane energy, $E_p = 2{P_K}^2/m_0$, where $P_K = -\mathrm{i}\,\langle \mathrm{S}|\hat{\mathrm{p}}_{\mathrm{z}}|\mathrm{Z}\rangle$ is the Kane momentum matrix element. This estimation is made using the expressions in Ref. [46,47], neglecting remote band contributions:

$$\gamma_2 \cong \frac{E_p}{6E_g} . \tag{S65}$$

In this expression we determine E_g from the measured exciton transition energy, $\hbar\omega$, as $E_g = \hbar\omega + \mathrm{B}_{1,0}$, where $\mathrm{B}_{1,0} = -\mathrm{E}_{1,0}(a_{10})$ is the binding energy of the lowest exciton, shown in Table S5. We determine the Kane energy from the oscillator strength per unit area measured for cleaved crystals reported in Table 1 of the main text, rather than from effective masses which are directly influenced by remote band effects. Using the results of Section S4, Eq. S35 and Eq S39 we solve for the Kane energy as [48],

$$E_p = \hbar\omega\,\frac{{f_\parallel}^{exc}}{S}\frac{1}{|\varphi_{10}(0)|^2}\frac{1}{cos^2\theta} . \tag{S66}$$

In this expression ${f_\parallel}^{exc}/S$ is the in-plane oscillator strength of the exciton, which is unaffected by the dielectric discontinuity in the 2D HOIP structure as described in Sec. S5. The term $|\varphi_{10}(0)|^2$ is the 2D exciton relative wavefunction evaluated at contact; from Eq S48 we evaluate this as $|\varphi_{10}(0)|^2 = 8/(\pi a_{10}^2)$. Finally, the phase angle θ reflects the Bloch function anisotropy in Eqs. 10-11; we determine this using Eq. S39 using the *intrinsic* ratio of the out-of-plane to the in-plane oscillator strength of the exciton as determined from the *measured* ratio via Eq. S43 in Section S5:

$$\tan\theta = \sqrt{\frac{1}{2}\left(\frac{{f_\perp}^{exc}}{{f_\parallel}^{exc}}\right)^{intrinsic}} . \tag{S67}$$

Using the numerical values for $\hbar\omega$ and the oscillator strength per unit area for polarization in-plane and out-of-plane tabulated in Table 1, the measured intrinsic ratio $({f_\perp}^{exc}/{f_\parallel}^{exc})^{intrinsic} = 0.166$ from Table S4, with the exciton radius $a_{10} = 3.3$ nm from Table S5, we find $E_p = 3.98$ eV, which compares favorably to the value $E_p = 5.5$ eV found for 4F-PEPI ($[\mathrm{pFC_6H_5C_2H_4NH_3}]_2\mathrm{PbI_4}$) in Ref. [22]. Using the calculated E_p, we calculate $\gamma_2 = 0.25$, which leads to an effective crystal field $\delta = -1.36$ eV using Eq. S64 with d = 0.644 nm. This is close to the corresponding value calculated using DFT for 4F-PEPI in

Ref. [22] , namely, $\delta = -1$ eV, where the negative sign is determined from analysis of the conduction band splitting in the absence of spin-orbit coupling in Ref. [22].

Given the effective crystal field splitting, the value of the intrinsic phase angle can be determined using Eq. S11 given the knowledge of the spin-orbit coupling parameter, Δ_{SO}; however, since this parameter is not known *a priori*, we adopt the converse approach of determining Δ_{SO} given the calculated crystal field and the measured oscillator strength ratio. Using the values summarized in Table S6 we obtain $\Delta_{SO} = 1.17$eV. As a check of the calculated value, we use Eq.s S61-63 to compute the average splitting between the band-edge energies of the heavy- and light-electron bands and the lowest conduction band:

$$\overline{\Delta} \equiv \bar{E}_{upper} - E^{c}_{\pm 1/2} = \frac{1}{4}\left(\delta + \Delta + \sqrt{9\delta^2 - 6\delta\Delta + 9\Delta^2}\right). \tag{S68}$$

Using the parameters above the average conduction band splitting at the Γ point splitting evaluates to $\overline{\Delta} = 1.50$ eV. For comparison the energy difference between the lowest conduction band and the average Γ point energy of the second and third conduction bands calculated using DFT-HSE+SOC (for which the band structure is shown in Figure S4) is $\overline{\Delta} = 1.53$ eV. Conversely, using $\overline{\Delta} = 1.53$ eV as determined using DFT-HSE+SOC, the spin-orbit coupling parameter evaluates to $\Delta_{SO} = 1.20$ eV, which matches the value $\Delta_{SO} = 1.2$ reported for 4F-PEPI in Ref. [22].

Table S6. Summary of parameters relevant to quantum well mixing model for PEPI.

Parameter	Value	Source
Measured intrinsic exciton anisotropy accounting for dielectric anisotropy$({f_z}^{exc}/{f_x}^{exc})^{intrinsic}$	0.166	Table S4
Bloch function phase angle, $\sin\theta$ from measured$({f_z}^{exc}/{f_x}^{exc})^{intrinsic}$	0.277	Eq. S39
Band gap E_g	2.644 eV	Table 1 and Table S5
Kane energy, E_p	3.98 eV	Eq. S66-S67 and Table 1
Luttinger parameter γ_2	0.25	Eq. S65
Effective crystal field, δ	1.36 eV	Eq. 64
Spin-orbit coupling parameter, Δ_{SO} calculated from measured $({f_z}^{exc}/{f_x}^{exc})^{intrinsic}$ and effective crystal field, δ	1.17 eV	Eq. S11 with measured $\sin\theta$
Spin-orbit coupling parameter, Δ_{SO} calculated from average conduction band splitting $\overline{\Delta} = 1.53$eV from DFT-HSE+SOC and effective crystal field, δ	1.20 eV	Eq. S68

Supporting Information References

[1] M. Campoy-Quiles, P. G. Etchegoin, and D. D. C. Bradley, *On the optical anisotropy of conjugated polymer thin films,* Phys. Rev. B - Condens. Matter Mater. Phys. **72**, 045209 (2005) http://doi.org/10.1103/PhysRevB.72.045209.

[2] J. P. Perdew, K. Burke, and M. Ernzerhof, *Generalized gradient approximation made simple,* Phys. Rev. Lett. **77**, 3865 (1996) http://doi.org/10.1103/PhysRevLett.77.3865.

[3] A. Tkatchenko and M. Scheffler, *Accurate molecular van der Waals interactions from ground-state electron density and free-atom reference data,* Phys. Rev. Lett. **102**, 073005 (2009) http://doi.org/10.1103/PhysRevLett.102.073005.

[4] D. B. Straus, N. Iotov, M. R. Gau, Q. Zhao, P. J. Carroll, and C. R. Kagan, *Longer Cations Increase Energetic Disorder in Excitonic 2D Hybrid Perovskites,* J. Phys. Chem. Lett. **10**, 1198 (2019) http://doi.org/10.1021/acs.jpclett.9b00247.

[5] K. Z. Du, Q. Tu, X. Zhang, Q. Han, J. Liu, S. Zauscher, and D. B. Mitzi, *Two-Dimensional Lead(II) Halide-Based Hybrid Perovskites Templated by Acene Alkylamines: Crystal Structures, Optical Properties, and Piezoelectricity,* Inorg. Chem. **56**, 9291 (2017) http://doi.org/10.1021/acs.inorgchem.7b01094.

[6] D. Ma, Y. Fu, L. Dang, J. Zhai, I. A. Guzei, and S. Jin, *Single-crystal microplates of two-dimensional organic–inorganic lead halide layered perovskites for optoelectronics,* Nano Res. **10**, 2117 (2017) http://doi.org/10.1007/s12274-016-1401-6.

[7] A. Fieramosca, L. De Marco, M. Passoni, L. Polimeno, A. Rizzo, B. L. T. Rosa, G. Cruciani, L. Dominici, M. De Giorgi, G. Gigli, L. C. Andreani, D. Gerace, D. Ballarini, and D. Sanvitto, *Tunable Out-of-Plane Excitons in 2D Single-Crystal Perovskites,* ACS Photonics **5**, 4179 (2018) http://doi.org/10.1021/acsphotonics.8b00984.

[8] X. Hong, T. Ishihara, and A. V. Nurmikko, *Dielectric confinement effect on excitons in PbI4-based layered semiconductors,* Phys. Rev. B **45**, 6961 (1992) http://doi.org/10.1103/PhysRevB.45.6961.

[9] N. Kitazawa, *Optical absorption and photoluminescence properties of Pb(I, Br)-based two-dimensional layered perovskite,* Japanese J. Appl. Physics, Part 1 Regul. Pap. Short Notes Rev. Pap. **36**, 2272 (1997) http://doi.org/10.1143/jjap.36.2272.

[10] B. Febriansyah, T. M. Koh, Y. Lekina, N. F. Jamaludin, A. Bruno, R. Ganguly, Z. X. Shen, S. G. Mhaisalkar, and J. England, *Improved Photovoltaic Efficiency and Amplified Photocurrent Generation in Mesoporous n = 1 Two-Dimensional Lead-Iodide Perovskite Solar Cells,* Chem. Mater. **31**, 890 (2019) http://doi.org/10.1021/acs.chemmater.8b04064.

[11] M. Era, S. Morimoto, T. Tsutsui, and S. Saito, *Organic-inorganic heterostructure electroluminescent device using a layered perovskite semiconductor (C6H5C2H 4NH3)2PbI4,* Appl. Phys. Lett. **65**, 676 (1994) http://doi.org/10.1063/1.112265.

[12] N. Kitazawa, M. Aono, and Y. Watanabe, *Temperature-dependent time-resolved*

photoluminescence of (C 6H 5C 2H 4NH 3) 2PbX 4 (X = Br and I), Mater. Chem. Phys. **134**, 875 (2012) http://doi.org/10.1016/j.matchemphys.2012.03.083.

[13] S. Neutzner, F. Thouin, D. Cortecchia, A. Petrozza, C. Silva, and A. R. Srimath Kandada, *Exciton-polaron spectral structures in two-dimensional hybrid lead-halide perovskites,* Phys. Rev. Mater. **2**, 064605 (2018) http://doi.org/10.1103/PhysRevMaterials.2.064605.

[14] Q. Zhang, L. Chu, F. Zhou, W. Ji, and G. Eda, *Excitonic Properties of Chemically Synthesized 2D Organic–Inorganic Hybrid Perovskite Nanosheets,* Adv. Mater. **30**, 1704055 (2018) http://doi.org/10.1002/adma.201704055.

[15] W. P. Huhn and V. Blum, *One-hundred-three compound band-structure benchmark of post-self-consistent spin-orbit coupling treatments in density functional theory,* Phys. Rev. Mater. **1**, 033803 (2017) http://doi.org/10.1103/PhysRevMaterials.1.033803.

[16] M. K. Jana, S. M. Janke, D. J. Dirkes, S. Dovletgeldi, C. Liu, X. Qin, K. Gundogdu, W. You, V. Blum, and D. B. Mitzi, *Direct-Bandgap 2D Silver-Bismuth Iodide Double Perovskite: The Structure-Directing Influence of an Oligothiophene Spacer Cation,* J. Am. Chem. Soc. **141**, 7955 (2019) http://doi.org/10.1021/jacs.9b02909.

[17] C. Liu, W. Huhn, K. Z. Du, A. Vazquez-Mayagoitia, D. Dirkes, W. You, Y. Kanai, D. B. Mitzi, and V. Blum, *Tunable Semiconductors: Control over Carrier States and Excitations in Layered Hybrid Organic-Inorganic Perovskites,* Phys. Rev. Lett. **121**, 146401 (2018) http://doi.org/10.1103/PhysRevLett.121.146401.

[18] A. V. Krukau, O. A. Vydrov, A. F. Izmaylov, and G. E. Scuseria, *Influence of the exchange screening parameter on the performance of screened hybrid functionals,* J. Chem. Phys. **125**, 224106 (2006) http://doi.org/10.1063/1.2404663.

[19] M. K. Jana, C. Liu, S. Lidin, D. J. Dirkes, W. You, V. Blum, and D. B. Mitzi, *Resolving rotational stacking disorder and electronic level alignment in a 2d oligothiophene-based lead iodide perovskite,* Chem. Mater. **31**, 8523 (2019) http://doi.org/10.1021/acs.chemmater.9b03208.

[20] R. S. Mulliken, *Electronic population analysis on LCAO-MO molecular wave functions. I,* J. Chem. Phys. **23**, 1833 (1955) http://doi.org/10.1063/1.1740588.

[21] M. Dyksik, S. Wang, W. Paritmongkol, D. K. Maude, W. A. Tisdale, M. Baranowski, and P. Plochocka, *Tuning the Excitonic Properties of the 2D (PEA)2(MA)n-1PbnI3 n+1Perovskite Family via Quantum Confinement,* J. Phys. Chem. Lett. **12**, 1638 (2021) http://doi.org/10.1021/acs.jpclett.0c03731.

[22] J. Even, L. Pedesseau, M. A. Dupertuis, J. M. Jancu, and C. Katan, *Electronic model for self-assembled hybrid organic/perovskite semiconductors: Reverse band edge electronic states ordering and spin-orbit coupling,* Phys. Rev. B - Condens. Matter Mater. Phys. **86**, 205301 (2012) http://doi.org/10.1103/PhysRevB.86.205301.

[23] P. C. Sercel, J. L. Lyons, D. Wickramaratne, R. Vaxenburg, N. Bernstein, and A. L. Efros, *Exciton Fine Structure in Perovskite Nanocrystals,* Nano Lett. **19**, 4068 (2019) http://doi.org/10.1021/acs.nanolett.9b01467.

[24] P. C. Sercel, J. L. Lyons, N. Bernstein, and A. L. Efros, *Quasicubic model for metal*

halide perovskite nanocrystals, J. Chem. Phys. **151**, 234106 (2019) http://doi.org/10.1063/1.5127528.

[25] Y. Nagamune, S. Takeyama, and N. Miura, *Exciton spectra and anisotropic Zeeman effect in PbI2 at high magnetic fields up to 40 T,* Phys. Rev. B **43**, 12401 (1991) http://doi.org/10.1103/PhysRevB.43.12401.

[26] T. Kataoka, T. Kondo, R. Ito, S. Sasaki, K. Uchida, and N. Miura, *Magneto-optical study on the excitonic spectrum of (C6H13NH3)2PbI4,* Phys. Rev B **47**, 4 (1993) http://doi.org/10.1103/PhysRevB.47.2010.

[27] K. Tanaka, T. Takahashi, T. Kondo, K. Umeda, K. Ema, T. Umebayashi, K. Asai, K. Uchida, and N. Miura, *Electronic and excitonic structures of inorganic-organic perovskite-type quantum-well crystal (C4H9NH3) 2PbBr4,* Japanese J. Appl. Physics, Part 1 Regul. Pap. Short Notes Rev. Pap. **44**, 5923 (2005) http://doi.org/10.1143/JJAP.44.5923.

[28] K. Ema, K. Umeda, M. Toda, C. Yajima, Y. Arai, H. Kunugita, D. Wolverson, and J. J. Davies, *Huge exchange energy and fine structure of excitons in an organic-inorganic quantum well material,* Phys. Rev. B - Condens. Matter Mater. Phys. **73**, 241310(R) (2006) http://doi.org/10.1103/PhysRevB.73.241310.

[29] L. Claudio Andreani, *Optical Transitions, Excitons, and Polaritons in Bulk and Low-Dimensional Semiconductor Structures,* in *Confin. Electrons Photons New Phys. Appl.*, edited by E. Burstein and C. Weisbuch (Springer US, Boston, MA, 1995), pp. 57–112 http://doi.org/10.1007/978-1-4615-1963-8_3.

[30] X. L. Yang, S. H. Guo, F. T. Chan, K. W. Wong, and W. Y. Ching, *Analytic solution of a two-dimensional hydrogen atom. I. Nonrelativistic theory,* Phys. Rev. A **43**, 1186 (1991) http://doi.org/10.1103/PhysRevA.43.1186.

[31] J. Pollmann and H. Büttner, *Effective Hamiltonians and binding energies of Wannier excitons in polar semiconductors,* Phys. Rev. B **16**, 4480 (1977) http://doi.org/10.1103/PhysRevB.16.4480.

[32] U. Rössler and H. R. Trebin, *Exchange and polaron corrections for excitons in the degenerate-band case,* Phys. Rev. B **23**, 1961 (1981) http://doi.org/10.1103/PhysRevB.23.1961.

[33] P. C. Sercel, Z. V. Vardeny, and A. L. Efros, *Circular dichroism in non-chiral metal halide perovskites,* Nanoscale **12**, 18067 (2020) http://doi.org/10.1039/d0nr05232a.

[34] E. L. Ivchenko and G. E. Pikus, *Superlattices and Other Heterostructures: Symmetry and Optical Phenomena, Superlattices and Other Heterostructures: Symmetry and Optical Phenomena*, 2nd Editio (Springer, 1997) http://doi.org/10.1007/978-3-642-60650-2.

[35] L. C. Andreani, *Exciton-polaritons in superlattices,* Phys. Lett. A **192**, 99 (1994) http://doi.org/10.1016/0375-9601(94)91023-5.

[36] R. A. Decrescent, N. R. Venkatesan, C. J. Dahlman, R. M. Kennard, M. L. Chabinyc, and J. A. Schuller, *Optical Constants and Effective-Medium Origins of Large Optical Anisotropies in Layered Hybrid Organic/Inorganic Perovskites,* ACS Nano **13**, 10745 (2019) http://doi.org/10.1021/acsnano.9b05504.

[37] R. R. Guseinov, *Coulomb Interaction and Excitons in a Superlattice,* Phys. Status Solidi B **125**, 237 (1984) http://doi.org/10.1002/pssb.2221250128.

[38] N. S. Rytova, *Screened potential of a point charge in a thin film,* Vestn. Moskow Univ. **3**, 30 (1967). Translated to English in https://arxiv.org/abs/1806.00976.

[39] L. Keldysh, *Coulomb interaction in thin semiconductor and semimetal films,* Jetp Lett. **29**, 658 (1979).

[40] E. Hanamura, N. Nagaosa, M. Kumagai, and T. Takagahara, *Quantum wells with enhanced exciton effects and optical non-linearity,* Mater. Sci. Eng. B **1**, 255 (1988) http://doi.org/10.1016/0921-5107(88)90006-2.

[41] E. A. Muljarov, S. G. Tikhodeev, N. A. Gippius, and T. Ishihara, *Excitons in self-organized semiconductor/insulator superlattices: PbI-based perovskite compounds,* Phys. Rev. B **51**, 14370 (1995) http://doi.org/10.1103/PhysRevB.51.14370.

[42] J. Even, L. Pedesseau, C. Katan, M. Kepenekian, J. S. Lauret, D. Sapori, and E. Deleporte, *Solid-state physics perspective on hybrid perovskite semiconductors,* J. Phys. Chem. C **119**, 10161 (2015) http://doi.org/10.1021/acs.jpcc.5b00695.

[43] J. C. Blancon, A. V. Stier, H. Tsai, W. Nie, C. C. Stoumpos, B. Traoré, L. Pedesseau, M. Kepenekian, F. Katsutani, G. T. Noe, J. Kono, S. Tretiak, S. A. Crooker, C. Katan, M. G. Kanatzidis, J. J. Crochet, J. Even, and A. D. Mohite, *Scaling law for excitons in 2D perovskite quantum wells,* Nat. Commun. **9**, 2254 (2018) http://doi.org/10.1038/s41467-018-04659-x.

[44] M. Gramlich, M. W. Swift, C. Lampe, J. L. Lyons, M. Do˙blinger, A. L.Efros, P. C. Sercel, and A. S. Urban, *Dark and Bright Excitons in Halide Perovskite Nanoplatelets,* Adv. Sci. **Accepted**, (2021) http://doi.org/10.1002/ADVS.202103013.

[45] J. M. Luttinger, *Quantum theory of cyclotron resonance in semiconductors: General theory,* Phys. Rev. **102**, 1030 (1956) http://doi.org/10.1103/PhysRev.102.1030.

[46] C. R. Pidgeon and R. N. Brown, *Interband magneto-absorption and faraday rotation in InSb,* Phys. Rev. **146**, 575 (1966) http://doi.org/10.1103/PhysRev.146.575.

[47] A. L. Efros and M. Rosen, *Electronic structure of semiconductor nanocrystals,* Annu. Rev. Mater. Sci. **30**, 475 (2000) http://doi.org/10.1146/annurev.matsci.30.1.475.

[48] M. W. Swift, J. L. Lyons, A. L. Efros, and P. C. Sercel, *Rashba exciton in a 2D perovskite quantum dot,* Nanoscale **13**, 16769 (2021) http://doi.org/10.1039/d1nr04884h.